New fault slip distribution for the 2010 M_w 7.2 El Mayor Cucapah earthquake based on realistic 3D finite element inversions of coseismic displacements using space geodetic data.

Fabio Pulvirenti[a], Zhen Liu[a], Paul Lundgren[a], Alejandro Gonzalez-Ortega[b], Marco Aloisi[c]

[a]Jet Propulsion Laboratory, California Institute of Technology, 4800 Oak Grove Dr, Pasadena, CA 91109, USA
[b]Departamento de Sismologia, Ciencias de la Tierra, CICESE, Mexico
[c] Istituto Nazionale di Geofisica e Vulcanologia, Osservatorio Etneo, Catania, Italy

Key point #1:
El Mayor Cucapah fault slip distribution is optimized in a realistic numerical environment to match geodetic data with minimal residuals.

Key point #2: Optimization with material heterogeneities fits better the observed deformation pattern with respect to the homogeneous case.

Key Point #3: Numerical results find no shallow slip on the southernmost fault plane.

Abstract

In this work we investigate the 4 April, 2010, M_w 7.2 El Mayor-Cucapah (EMC) earthquake. Existing studies modeled the EMC area as an elastic half-space in a homogeneous or vertically layered structure, which, along with differences in data and inversion methodologies, led to considerable variability in the resultant fault slip models. To investigate the EMC earthquake more realistically, we first examine how published coseismic fault slip models have approached the problem and what are their findings, then we select the optimal geometry and slip of one most recent and comprehensive coseismic fault slip model, obtained through analytical inversions, and adapt them in a three-dimensional finite element numerical environment where we assess the effects of topography and material heterogeneities. Numerically optimized slip models are obtained via joint inversion of GPS, interferometric synthetic aperture radar and subpixel offset datasets. We find the effect of topography to be negligible while the inclusion of material heterogeneities enhances the slip at depth, as might be expected where the medium has higher rigidity, and better fits the displacements at both near and far field, especially around the Salton Sea area. The match with geodetic data is significantly improved when the fault slip is increased at the fault planes close to the epicenter and deeper at the southernmost plane, with respect to the slip of the chosen

analytical model. Our findings suggest that this earthquake was associated with a higher and more spatially concentrated slip than previously thought implying a greater stress drop at depth.

1. Introduction

The 4 April 2010 El Mayor Cucapah (EMC) earthquake struck northeastern Baja California, near the border between California and Mexico. This area is characterized by several transform faults which accommodate the relative motion between the Pacific and North American plates, with the former moving NW at a rate of ~48-52 mm/year (Argus et al., 2010; DeMets et al., 2010) with respect to the latter. As pointed out by Fletcher et al. (2014), multifault ruptures in the area are the result of different mechanisms including restraining bend tectonics, gravitational potential energy gradients, three-dimensional strain of the transtensional and transpressional shear regimes. The EMC epicenter was located at Long.=-115.27° and Lat.=32.30°, according to the Southern California Seismic Network (SCSN) catalog. With M_w=7.2 (https://www.globalcmt.org), this is one of the larger seismic events (M_w >6) that has occurred in the area since 1987 (Spinler et al., 2015; Gonzalez-Ortega et al., 2018). Its occurrence caused damage to roads, buildings and power lines in the city of Mexicali, with extensive damage also reported throughout agricultural areas (Stenner et al., 2010). A comprehensive report has been released by Meneses et al., 2010 (EERI Report No. 2010-02). The EMC earthquake is peculiar for two main reasons: 1) it was characterized by a bidirectional rupture extending more than 120 km along strike and oriented NW-SE; 2) radar interferometry, seismicity, field measurements and creepmeters (Hauksson et al., 2011; Fletcher et al., 2014; Gonzalez-Ortega et al., 2014) reveal that this event activated more fault segments than any other prior event in the area: Pescadores, Borrego, Paso Inferior, Paso Superior in the northwest and the Indiviso to the southeast (rather than the expected seismogenic Cerro Prieto fault). To the north in California, numerous faults were also involved: the San Andreas, Superstition Hills, Imperial, Elmore Ranch, Wienert, Coyote Creek, Elsinore, Yuha and several minor faults near the town of Ocotillo (Wei et al., 2011b; Kroll et al., 2013; Donnellan et al., 2014). Fault motion was mainly right-lateral strike with some normal component. The EMC earthquake is also thought to be responsible for increasing the gas flux of a series of mud volcanoes located near the Salton Sea (Rudolph and Manga, 2010); in particular, these authors suggest that strains up to 1.2%, induced by the earthquake near the mud volcano location, may have increased the permeability, which in turn affected the volcano degassing activity. Trugman et al., (2014) observed that anthropogenic fluid extraction at Cerro Prieto Geothermal Field site (at approximately 15 km NE of EMC epicenter) may have contributed to destabilizing the area before the earthquake by generating positive Coulomb stress rates on the order of 15 kPa/yr near the hypocenter and so exceeding the local

tectonic stressing rate. The main shock was followed by numerous aftershocks around the epicenter, defining a seismogenic zone extending to a depth of about 10 km (Castro et al., 2011).

1.1 Previous studies

Several authors have studied this event through analytical and numerical inverse modeling of different sets of data, such as teleseismic body waves, GPS, interferometric synthetic aperture radar (InSAR) and subpixel offsets, in order to characterize the number of fault segments involved and the fault slip distribution. Results show that measured geodetic data require assuming the existence of a NW-SE oriented multi-segment fault system, with each segment having variable strike and dip angles. Despite the detailed observations of the fault trace at the surface obtained from geological (Fletcher et al., 2014) or differential LIDAR measurements (Oskin et al., 2012), there is no general agreement on the number of fault segments actually involved. For example, Wei et al. (2011a) performed joint inversions of geodetic, remote-sensing and seismological data using a simulated annealing algorithm, obtaining the best match using a 4-segment fault geometry. Uchide et al., (2013) inverted strong motion data to infer the slip distribution on a 6-segment fault geometry, while joint inversions of SAR, optical and GPS (continuous and campaign) data by Fialko et al. (2010) suggested the presence of 7 fault segments. Finally, the analytical joint inversions of GPS, InSAR and subpixel offset data by Huang et al. (2017, hereafter Huang17) indicated a geometry composed of 9 fault segments (Fig. 1). Most of these studies were based on simplified assumptions that underestimate the complexity of the area, often represented as a half space with no topography. Moreover, no interaction is assumed to exist between adjacent fault planes and the medium is treated as elastically homogeneous or, in some cases, as vertically stratified. These assumptions might lead to biases in the estimation of the amount and distribution of slip at depth. Hauksson et al. (2015) show for example that at depth, under the NW-SE fault rupture profile, there is a strong variation of V_p and this suggests that accounting for full heterogeneities (vertical and lateral) may be a viable way to better reproduce the correct response of the medium. In order to understand if the existing assumptions are sufficient to describe the event or can rather jeopardize its interpretation, we performed a 3D finite element model inverting GPS, InSAR and subpixel offset data from Huang17, assessing the contribution of topography and full heterogeneities. In Section 2, we describe the model. In Section 3, we present the data. In Section 4 we show the results. In Section 5, we discuss our findings and provide conclusions.

2. Model

To study the EMC, we develop a finite element method (FEM) model and its solution using the commercial software COMSOL Multiphysics v5.4. The model represents an area extending from the northeast tip of the Gulf of California to the Mojave Desert (Fig. 1, inset). This extent allows us to include a consistent number of GPS stations in both the US and Mexico, and to take into consideration the area covered by the InSAR and optical observations as well. The area is numerically represented by a 540x440 km 3D domain which extends to 150 km depth (Fig. 2a). The main domain is framed by a set of domains that are further extended numerically using an "*infinite element"* setting. The infinite element applies a real-valued coordinate scaling (or stretching) to the domains surrounding the physical region of interest and having coincident nodes. The domains are scaled by default to be very much larger than the original geometry and the finite distance to the far-away boundary allows prescribing standard boundary conditions. By stretching the domains, we avoid possible boundary effects which could arise from a premature truncation. Into the main domain, the fault system (Fig.1) is embedded following the geometry suggested by Huang17. The fault system consists of 9 shell-type fault planes with different strike and dip angles and a maximum depth of 16 km below the top surface (Fig. 2a). Embedding the fault planes into a continuum domain overcomes the need of building complex twisted noncoplanar connecting surfaces, still assuring the interaction between adjacent planes and the continuity of the displacement field without forcing *a priori* geometrical connections between the different fault segments. Topography is included using a digital elevation model (DEM) from the Shuttle Radar Topography Mission (SRTM) data with 30 m resolution (https://www2.jpl.nasa.gov/srtm/). In particular, DEM data are imported and included in the model in the form of a "*parametric surface"*, where the parameter is the DEM elevation mapped to a series of points on the domain top surface, generating a realistic topography (Fig. 2b). No bathymetry is used. In terms of material properties, the medium can be treated as elastically homogeneous or with vertical heterogeneities (layered) or with vertical plus lateral heterogeneities (hereafter, heterogeneous). For the first two cases, we adopt the same parameters given by Huang17 in their table S2. The layered case considers a vertically variable Young's modulus (Fig. 2b) and a constant Poisson's ratio of 0.25 while full heterogeneities (Fig. 2c, 2d) are obtained using the V_p, V_s and density data from the SCEC Community Velocity Model Harvard v15.1.1 (https://scec.usc.edu/scecpedia/CVM-H) and converting them into elastic moduli using the Christensen and Mooney (1995) empirical law. Material parameters are summarized in Table 1. Because the model is kinematic, density is not relevant. The mesh for the domain volumes is composed of tetrahedral elements while the outside boundaries are discretized using triangular elements. At the top surface, the mesh is finer in proximity of the fault trace and becomes coarser

144 away from the area of interest (Fig. 3a). Fault planes along the fault trace are discretized into 432
145 patches using quadrilateral elements of about 2x2 km, in order to have a regular mesh and better
146 control on the fault slip distribution, while triangular elements are used for the transverse plane to
147 better control its intersection with one of the planes along the fault trace (Fig. 3b). We assign 1 m
148 slip to each fault plane and perform direct mesh sensitivity tests in order to find a reasonable
149 balance between the mesh quality and a solution which does not change with further refinements.
150 The domain top surface is stress-free while the bottom is fixed. A roller condition (no displacement
151 in the normal direction) is applied at the side boundaries. Fault segments are treated with the so
152 called "*thin elastic layer"* condition and a prescribed slip (right-lateral and dip-slip components, as
153 suggested by Huang17). The thin elastic layer condition allows having two sets of coincident mesh
154 nodes for the two sides of the shell. We perform a joint optimization of GPS, optical and InSAR
155 data using the gradient based optimization algorithm SNOPT (Gill et al., 2005), available in
156 COMSOL. Details about SNOPT are given in paragraph S2 of the Supporting Information.
157

158 ## 3. Input Data

159

160 Recorded geodetic data are taken from Huang17 (see their supplementary material). In particular,
161 three sets of geodetic data are used in our model: GPS, InSAR and subpixel offsets
162 (https://doi.org/10.5281/zenodo.4290782). GPS data consist of 23 near field stations installed on the
163 Mexican side by the researchers of the Centro de Investigación Científica y de Educación Superior
164 de Ensenada (CICESE) a few days after the event and 132 near to far field PBO stations from the
165 UNAVCO Data Center, located on the US side. InSAR data consist of a total of 4433 down-
166 sampled points from ascending and descending tracks of ALOS PALSAR and ENVISAT ASAR
167 SAR sensors. For each point, Huang17 provided longitude, latitude, azimuth, view-angle and value
168 along the satellite line-of-sight (LOS). We convert azimuth and view angle into the three direction
169 cosines, in order to project the model top surface displacements into the LOS. Subpixel offset data
170 include SPOT5 satellite optical image pair for the E-W and N-S components at 293 points. Starting
171 from the geometry and slip reported in Huang17 (see their Supplementary Material Table S1), we
172 first validate the FEM model by checking that the numerical output at selected GPS stations is
173 consistent with the output obtained analytically, using Okada (1985) type dislocations (see
174 Supplementary material Fig. S1). Once the model has been validated, we assess if, for the same slip
175 distribution, the model predictions at the GPS sites show a good fit compared to the recorded
176 coseismic displacements. The results show that the vectors obtained using the slip from Huang17 do
177 not fit perfectly with the measurements (Fig. 4a). In particular, while globally the two solutions

show vectors with similar orientation (except for a few stations), the vectors obtained using the slip from Huang17, underestimate (up to 40%) the measurements in both horizontal and vertical components at almost all stations (Fig. 4b). Therefore, with our numerical approach, we use Huang17 slip distribution solution as an initial guess to guide the model and then perform a joint inversion in the more realistic FEM computational environment. The goal is to find a new slip distribution whose output better fits the observations. Details on the inversion methodology are provided in paragraph 2 of the supplementary material.

4 Results

In this section, we compare the output at the model top surface, obtained from our joint optimization, to the recorded GPS, InSAR and subpixel offset datasets. Residuals and standard deviation are also calculated for all cases (Table 2) and compared to the one obtained from the Huang17 solution.

4.1 Comparison with GPS data

Figure 5a and 5b show the comparison between the predicted (numerically optimized) solution and the observed surface displacements for the homogeneous case. For visualization purposes, the comparison is restricted to the near field GPS stations east of the fault trace, which are the ones showing significant horizontal displacements of several centimeters. These include 17 Mexican stations and 4 PBO stations. Comparing Figures 5a and 5b with Figures 4a and 4b, we see that the optimized slip solution produces predicted displacements in better agreement with the observations. Error ellipses are not shown because the associated error for the GPS stations is about 4 mm and won't be visible at the chosen scale. Slight misalignments appear at BG51 and VM15 stations. This appears to be an effect of the joint inversion, since the model must fit with a reasonable balance three sets of data. Not surprisingly, when we invert for the GPS data only (see Supplementary Material figure S3) a better fit is obtained at these stations.

Next, we examine the effects of layered and heterogeneous structure. Figure 6a extends the results of Figure 5a including the displacement vectors obtained from the joint inversion for the layered and heterogeneous case. All solutions have a coherent SE pattern with respect to the recorded data, which is consistent with the expected direction of displacement on the eastern side of the fault (since the slip is right-lateral strike). The vectors belonging to the homogenous solution being slightly bigger (about 1 cm) than the layered and heterogeneous solutions, as can be seen in their difference vectors (Fig. 6b). A similar discrepancy (1-2 cm) between the length of the vectors of the

homogeneous solution versus the ones for the layered and heterogeneous can also be observed in the far field in the area around the Salton Sea (Fig.7a). In both cases, (near and far field) we see that the homogeneous solution vectors over-predict the observed displacements. This result is in line with the geology of the area. As shown in Rollins et al., (2015) (see their Fig 1a), the area near the Salton Sea belongs to the Salton Through, a region featuring a shallow lithosphere–asthenosphere boundary and shallow Moho and distinct from the surrounding area of the Peninsular Ranges. Our solutions (layered and heterogeneous) are able to capture these differences giving vectors closer to the measurements, while the use of a homogeneous domain would produce a systematic misfit. However, since the layered and heterogeneous solutions produce very similar vectors (blue and gray vectors almost overlap), we can conclude that the differences described above are mostly driven by the vertical heterogeneities rather than the horizontal ones. Vertical components are captured almost equally showing an uplift south of the Salton Sea, as expected. Comparisons between the Huang17 solution and our solution for all GPS stations in terms of standard deviation (Table 2) shows that numerical joint optimization improves the total standard deviation by about 50%.

4.2 Comparison with InSAR data

Referring to the same area as in Figure 1, Figure 8 shows the measured, modeled and residual (measured-modeled) results for the InSAR ascending and descending tracks in the homogenous case. The comparison shows that the homogeneous joint inversion fits well with the recorded data so that residuals are close to zero. The difference (residuals) between predictions of models assuming homogeneous and layered structure (H-L) or homogeneous and heterogeneous structure (H-He) for the ascending and descending tracks are shown in Figure 9. For both cases, the inclusion of heterogeneities implies changes in the range of ±0.05 m. The H-He case produces slightly larger residual values with respect to the H-L case, which means that, as found for the GPS data, that the output obtained for the heterogeneous case is lower in magnitude than the layered one. Quantifications in terms of standard deviation for all material configurations are shown in Table 3. Numerical optimization improves the standard deviation of InSAR data by 45% for the ascending track and by 22 % for the descending track with respect to Huang17 solution.

4.3 Comparison with subpixel offset data

Referring to the same area as in Figure 1, Figure 10 shows the measured, modeled and residual results for the subpixel offset datasets EW component (top row) and NS component (bottom row) in

247 the homogenous case. When we look at the residual for the EW component, most points drop to
248 about zero values, however we can also notice that some of them in the very north and central part
249 of the fault shows values in the range ±0.5 m. Residuals for the NS component appear instead more
250 uniform with values between 0 and -0.3 m. Figure 11 shows the residuals of the H-L and H-He
251 model predictions, the latter giving slightly higher values. Globally, residuals from the FEM
252 solutions are in the range of ±0.05 m for the EW component and ±0.10 m for the NS component.
253 Quantifications in terms of standard deviation for all material configurations are shown in Table 4.
254 Numerical optimization improves the total standard deviation by 10% with respect to the analytical
255 solution.
256
257 **4.4 Non optimized vs optimized slip distribution**
258
259 Figure 12 shows the slip distribution on the fault planes. The not optimized slip (Fig.12a) which
260 corresponds to the solution from Huang17, is compared to the optimized slip in the homogeneous,
261 layered and heterogeneous domains (Fig. 12b, 12c and 12d, respectively). Qualitatively we can
262 observe that, as a result of the optimization, the slip is increased in all planes. For a better
263 understanding we assign a number to each plane with the leftmost plane being the plane number 1
264 and rightmost the plane number 8. The 40° E transverse plane is number 9. The increase with
265 respect to the starting solution is clearly observed at the top part of plane 2 (in correspondence to
266 the Borrego fault), at planes 4 and 5 (in correspondence to the Pescadores fault), at the top right part
267 of plane 6 and at plane 8 (Indiviso fault). Moreover, the slip on plane 8 is centered at about 8 km
268 depth in our FE optimized joint solution, which is deeper than the solution found through analytical
269 joint inversions by Huang17, where the slip appears to be centered at above 5 km depth. Slip on
270 plane 9 is shown only for the Huang17 solution, because it is similar for all cases. In particular,
271 about 1 m, quite uniform slip is found on this plane, which is consistent with an unfavorably
272 oriented fault with respect to the regional stress field, as pointed out by Fletcher et al. (2016). The
273 layered and heterogeneous solution (Figure 12c and 12d) shows higher slip at depth (especially on
274 plane 6) with respect to the homogeneous case (Figure 12b). This is consistent with the higher
275 rigidity of the medium at depth combined with the plane position and dip angle. The vertically
276 stratified (layered) and the 3D heterogeneous models however have a more similar slip distribution.
277 Figure 13 helps to quantify the differences between the different cases. Figure 13a shows the
278 residual between the slip distribution before (Huang17) and after the optimization in the
279 homogeneous domain. We can observe an increase of the slip by up to 3 meters and that the slip
280 distribution is more compact on planes 2, 4 and 8 while all of plane 5 is required to slip. Figure 13b

shows the residual between the layered and the homogeneous numerical solutions. An increase of 1-2 meters is observed at depth on plane 6 while in some areas the increase is between 0.5 and 1 m. These last however, appear to be too sporadic to infer a uniform slip and we think that they are a combined effect of the material properties and the plane's dip angle. Figure 13c shows the residual between the heterogeneous and the homogeneous cases. Because the slip for the layered and heterogeneous solutions are similar Figure 13c is similar to Figure 13b, and in turn the residual between the slip distributions for the layered and the heterogeneous cases (Fig 13d) are very similar, with minor differences in the ±1 m range.

Our tests indicate that when we start from Huang17 joint slip solution and perform the numerical inversions, the slip on plane 8 becomes greater and deeper when InSAR data are included in the joint inversion, while it remains unchanged (same as starting solution) if the inversion is performed considering the GPS data only (see figure S4 in Supplementary Material). We would expect a similar finding from Huang17 during the inversion of the InSAR data (which are the only data available in that area) instead, in their Figure 4, the authors show that a slip higher than 5 m appears on the southernmost plane when subpixel offset data (only) are inverted while, in the inversion for InSAR data only, their slip on plane 8 looks deeper and having a value of about 2 m. This means that, in their joint solution, the strong slip on plane 8 is driven by the subpixel offset data, however because these data are obtained combining InSAR and Optical datasets, with the latter being only to the north of the epicenter, there are no subpixel offset data to the south and, therefore, it is more reasonable to find slip on that plane when InSAR data are considered, as in our case. In order to understand the effect of the initial guess on the slip distribution of plane 8 in the joint numerical solution, we performed an additional test keeping the solution from Huang17 as the initial guess in all planes expect plane 8, where we assume instead a uniform slip of 1 m on plane 8 at the beginning of the optimization. When we do so, the model finds again a slip similar to the one we obtain using the Huang17 solution as the starting guess. This time its value is smaller (about 5 m) and also has a shallower appendix on top (Fig.14). We will call this solution intermediate slip, where intermediate is to be intended as intermediate depth to discriminate from the deeper one. Even though it's hard to have high level confidence about the slip distribution at depth on this plane (because the inversion depends only on few pixels of the InSAR dataset), our checkerboard tests (see Supplementary material Figures S2) prove that our model is capable to reasonably resolve a predefined slip distribution when inverting for the top surface data (even perturbed) so we can exclude the effect of numerical artefacts in the solution. The results obtained for both cases suggest that a very shallow slip (close to the fault trace) is unlikely to occur and this is in line with what was observed in the field in this area, where the fault trace appears sporadic (Fletcher et al., 2014). To

see which solution (deep or intermediate) would be more in line with existing data, we cross-checked the output of the two solutions at the GPS stations located at the western side of the fault trace, which are mostly affected by the northwestward motion of the fault. Figure 15 shows that the solution with the deeper and strong slip (red vectors) and the one with intermediate and weaker slip (blue vectors) are similar. This is because, in both cases, the model has to fit the recorded data, so that in the intermediate slip case, the value is smaller than the deeper solution. A comparison at SALD (which is the station closest to the plane) shows that the intermediate slip produces a vector whose orientation is slightly closer to the observation. The solutions with a deeper or intermediate slip on the southernmost plane are also compared in terms of residuals with the recorded data for the InSAR (Fig.16). We can observe that in the intermediate slip case, a slightly lower residual is visible near the SE tip of the fault trace. No comparison is necessary with the subpixel offset data, because there are no subpixel offset data near plane 8. Independent calculations, as the one performed by Fialko et al. (2010) or Kyriakopoulos et al. (2017) (preferred model) also exclude very shallow slip on plane 8. This agreement is noteworthy because greater slip at depth is important for postseismic afterslip and relaxation analyses and may also have implications for dynamic fault models and aftershock generation. Finally, to understand if our slip distribution is reasonable, we calculated the seismic moment and the corresponding moment magnitude M_w using the following formula:

$$M_0 = \mu * D * A \quad (1)$$

$$M_w = \frac{2}{3}(Log(M_0) - 6.04 \quad (2)$$

where μ is the shear modulus, D the slip and A the fault plane area. We obtain the results shown in Table 5, with a moment magnitude close to the GCMT value.

5. Discussion and Conclusions

In this work we investigate the coseismic displacements of the El Mayor Cucapah earthquake. Because of the complexity of this event, related to the number, location and kinematics of the activated fault segments, several interpretations of the slip distribution (obtained from the inversion of different geodetic datasets) exist. Prior studies show that the variability of the interpretation depends on the data sets used and the underlying assumptions, such as the use of a flat stress-free surface, instead of a realistic topographic relief, and/or a simplified characterization of the real material properties. We choose one of the most complete published results, obtained through

analytical inversions by Huang17, as a starting point (same fault planes configuration and same reported slip) for our model and use the capability of the numerical (finite element) approach to test the goodness of the corresponding output when adding additional complexity (e.g. the presence of topography) and further optimizing the slip distribution using different material configurations. We first perform a series of direct tests. Our direct tests show that the numerical model can reproduce the output obtained analytically for a dislocation in a halfspace, so no artificial numerical effects exist due to the chosen geometry and level of discretization (mesh). When topography is used, the numerical output produces minor changes (less than 2%) with respect to the flat case, a result which is consistent with the low topographic relief of the area and is in line with other independent analyses (Kyriakopoulos et al., 2017). The effects of topography are found to be small even in cases where topographic variations are substantial (e.g., Wang and Fialko, 2018). For this reason, topography is neglected in the subsequent analyses. The use of the Huang17 solution in a direct numerical model generates near field GPS displacement vectors which underestimate the observed data.

To improve the fit in the near field and take into consideration the data in the far field, we start from the solution of Huang17 as an initial guess to guide the model, and use all the available geodetic datasets (GPS, InSAR and subpixel offset) to perform joint numerical inversions, taking into account the contribution from different material configurations (including vertical and vertical plus lateral heterogeneities). Preliminary checkerboard tests prove that the method used for the inversion is reasonably robust. Results of our finite element joint inversions show that higher slip is required on the central planes near the epicenter, with respect to the slip distribution reported by Huang17, to get a good match with recorded GPS data. A good fit is also found against the InSAR and subpixel offset data, with minimal residuals. The comparison between the different surface displacements obtained from the homogeneous, layered and heterogeneous material configurations shows that all solutions have a coherent pattern and that using a homogeneous material gives greater displacements, with the layered being intermediate in magnitude and the heterogeneous being the smallest. Since the heterogeneous case is the most realistic case, this means that limiting the analysis to a homogeneous or layered material (as in most of the analytical approaches) may introduce a systematic misfit in the estimation of the computed surface displacements, while with the numerical approach we are able to detect and overcome this limitation and better fit the observed displacements. This is particularly evident when we look at the displacement vectors in the Salton Trough area where the solution corresponding to the inversion performed with a layered or heterogeneous model captures better the displacement field with respect to the homogeneous case. Compared to other models, our slip distribution has similarities but also differences. Similar to

Fialko et al., (2010), Wei et al. (2011) Kyriakopoulos et al. (2017) and Huang et al. (2017) most of the slip is found near the epicenter (Pescadores Fault) and at the end of the Indiviso fault. However, in the preferred model of Kyriakopoulos et al. (2017), the slip from the Pescadores Fault to the Borrego Fault does not show any interruption while we are able, instead, to find a good correspondence with areas having low or no slip like the PIAZ and PAZ accommodation zones (Figures 1 and 12). Our joint inversions also show a greater and deeper slip at the southernmost plane, with respect to the starting solution of Huang17. However, since the Huang17 solution on plane 8 seems to be driven mostly by subpixel offsets rather than InSAR, we performed one additional test without using Huang17 as the starting solution on this plane. Results confirm that when we start from a 1 m uniform slip, a deeper slip still appears as an effect of the InSAR data, which means that the result is somehow consistent with our previous finding. However, in this second case, the slip is slightly more extended (with a shallower part) and smaller than the numerical solution obtained using Huang17 as the initial guess. To check which of the two solutions (intermediate or deep) is preferred, we test the outputs of both solutions on the GPS stations located west of the fault trace, which are the ones mostly affected by the three westward dipping planes (southward of the epicenter) and we compare these outputs to the measured data. The GPS vectors on SALD, which is the station closest to the southernmost fault plane are in favor of the solution with the intermediate slip. A slightly better agreement is also found with InSAR data when the solution with the intermediate slip is chosen. In both cases, a very shallow slip is excluded. Two aspects which may support the absence of a very shallow slip are the absence of a clear fault trace in that area (which would be expected if the slip is close to the surface) and the correspondence to other studies, which also found the slip to be deeper (Fialko et al. 2010, Kyriakopoulos et al. 2017). Finally, our slip values and distributions are consistent with the expected moment magnitude and close to the GCMT solution (max difference is about 2%) which means that the slip distributions we found are also quantitatively reasonable. Because we use the same fault geometries as Huang17 but we obtain a different slip distribution with our FEM optimization, even when using the same homogeneous material properties, we can exclude that the difference between their and our slip distribution is due to differences in the fault position and/or orientation or in a different response of the medium and we speculate that instead the differences between our slip distribution and theirs may be due to differences in their inverse method with respect to ours. In particular, the use of an optimization algorithm tailored for a numerical environment, rather than an analytical one, may be the cause of the improved fit to the recorded data and the high confidence we obtain, which can provide new clues to better understand the dynamics of such a complex event.

Acknowledgements

Starting slip distribution, GPS, InSAR and optical data are from Huang et al., (2017) (see their Supporting Information S1 and Data Set S1, S2 and S3 respectively). The data used as input in our model plus the slip distribution obtained by our joint inversions are available online at the following link: https://doi.org/10.5281/zenodo.4290782 .

The SCEC community velocity model is available at the website: https://scec.usc.edu/scecpedia/CVM-H. The topography data are available at the website: https://www2.jpl.nasa.gov/srtm/. The authors wish to thank: Mong Han Huang (University of Maryland) and Eric Fielding (JPL) for the fruitful discussions about the differences between the analytical and the numerical solution. Adriano Gualandi (JPL) for the support with the analysis of the analytical data. Francesco Guglielmino and Flavio Cannavò (INGV) for the assistance with data implementation. Egill Hauksson (Caltech) for the discussion about seismicity data. This work was carried out at the Jet Propulsion Laboratory (JPL), California Institute of Technology, under a contract with the National Aeronautics and Space Administration. The research was supported by an appointment to the NASA Postdoctoral Program at the Jet Propulsion Laboratory, California Institute of Technology, and administered by Universities Space Research Association under contract with NASA, in collaboration with the Agenzia Spaziale Italiana (ASI).

References

Argus, D. F., R. G. Gordon, M. B. Heflin, C.Ma, R. J. Eanes, P. Willis,W. R. Peltier, and S. E. Owen (2010). The angular velocities of the plates and the velocity of Earth's centre from space geodesy, Geophys. J. Int. 180, no. 3, 913–960. https://doi.org/10.1111/j.1365-246X.2009.04463.x

Castro, R. R., Acosta, J. G., Wong, V. M., Perez-Vertti, A., Mendoza, A., & Inzunza, L. (2011). Location of aftershocks of the 4 April 2010 M_W 7.2 El Mayor-Cucapah earthquake of Baja California, Mexico. Bulletin of the Seismological Society of America, 101(6), 3072–3080. doi: 10.1785/0120110112

Christensen NI, Mooney WD (1995) Seismic velocity structure and composition of the continental crust: a global review. J Geophys Res 100:9761–9788. https://doi.org/10.1029/95JB00259

G. B. Dantzig, Linear Programming and Extensions, Princeton University Press, Princeton, New Jersey, 1963.

DeMets, C.,R. Gordon, D. Argus (2010). Geologically current plate motions. *Geophysical Journal International*, Volume 181, Issue 1, April 2010, Pages 1–80, https://doi.org/10.1111/j.1365-246X.2009.04491.x

Donnellan, A., J. Parker, S. Hensley, M. Pierce, J. Wang, and J. Rundle (2014), UAVSAR observations of triggered slip on the Imperial, Superstition Hills, and East Elmore Ranch Faults associated with the 2010 M 7.2 El Mayor-Cucapah earthquake, Geochem. Geophys. Geosyst., 15, 815–829, doi:10.1002/ 2013GC005120.

Fialko, Y., Gonzalez, A., Gonzalez-Garcia, J. J., Barbot, S., Leprince, S., Sandwell, D. T., & Agnew, D. C. (2010). Static rupture model of the 2010 M7.2 El Mayor-Cucapah Earthquake from ALOS, ENVISAT, SPOT and GPS Data, pp. B2125. Pasadena, CA: American Geophysical Union, Fall Meeting.

Fletcher, J. M., Teran, O. J., Rockwell, T. K., Oskin, M. E., Hudnut, K. W., Mueller, K. J., et al. (2014). Assembly of a large earthquake from a complex fault system: Surface rupture kinematics of the 4 April 2010 El Mayor–Cucapah (Mexico)M_W 7.2 earthquake. Geosphere, 10(4), 797 – 827. https://doi.org/10.1130/GES00933.1

Fletcher, J., Oskin, M. & Teran, O. The role of a keystone fault in triggering the complex El Mayor–Cucapah earthquake rupture. *Nature Geosci* **9,** 303–307 (2016). https://doi.org/10.1038/ngeo2660.

P.E. Gill, W. Murray, and M.A. Saunders, "SNOPT: An SQP Algorithm for Large-Scale Constrained Optimization", SIAM Review, vol. 47, no. 1, pp. 99–131, 2005.

Gill P., Murray W., Saunders A., 2006. User's Guide for SNOPT Version 7: Software for Large-Scale Nonlinear Programming. Stanford University - Business Software Inc.

Gonzalez-Ortega J.A., Gonzalez-Garcia J., Sandwell D. Interseismic Velocity Field and Seismic Moment Release in Northern Baja California, Mexico. Seismol. Res. Lett. 2018. 89 (2A). https://doi.org/10.1785/0220170133

González-Ortega, A., Fialko, Y., Sandwell, D. T., Alejandro Nava-Pichardo, F., Fletcher, J., González-García, J. J., et al. (2014). El Mayor-Cucapah (M_W 7.2) earthquake: Early near-field postseismic deformation from InSAR and GPS observations. Journal of Geophysical Research: Solid Earth, 119, 1482–1497. https://doi.org/10.1002/2013jb010193.

Hauksson, E. J. Stock, K. Hutton, Y. Wezheng, A. V. Villegas, and H. Kanamori (2011). The 2010 M_w 7.2 El Mayor-Cucapah Earthquake Sequence, Baja California, Mexico and Southernmost California, USA: Active Seismotectonics along the Mexican Pacific Margin. Pure Appl. Geophys. 168, 1255-1277. doi:/10.1007/s00024-010-0209-7

Huang, M. H., Fielding, E. J., Dickinson, H., Sun, J., Gonzalez-Ortega, A., Freed, A. M., & Bürgman, R. (2017). Fault geometry inversion and slip distribution of the 2010 M_W 7.2 El Mayor-Cucapah earthquake from geodetic data. Journal of Geophysical Research: Solid Earth, 122, 607–621. https://doi.org/10.1002/2016JB012858.

Kyriakopoulos, C., Oglesby, D. D.,Funning, G. J., & Ryan, K. J. (2017). Dynamic rupture modeling of the M7.2 2010 El Mayor-Cucapah earthquake: Comparison with a geodetic model. Journal of Geophysical Research: Solid Earth, 122, 10,263–10,279. https://doi.org/10.1002/2017JB014294

Kroll K.A., E.S. Cochran, K.B. Richards-Dinger, D.F. Sumy. Aftershocks of the 2010 Mw 7.2 El Mayor-Cucapah earthquake reveal complex faulting in the Yuha Desert, California. 2013. https://doi.org/10.1002/2013JB010529

Meneses J.F., Hutchinson T.C., Hoehler M., Watkins D., and R. Wood. (2009). The El Mayor Cucapah, Baja California Earthquake April 4, 2010. Report number: EERI Report No. 2010-02

Okada, Y., 1985. Surface deformation due to shear and tensile faults in half-space. Bull. Seismol. Soc. Am. 75, 1135–1154.

Oskin, M. E., Arrowsmith, J. R., Corona, A. H., Elliott, A. J., Fletcher, J. M., Fielding, E. J., et al. (2012). Near-field deformation from the El Mayor-Cucapah earthquake revealed by differential LIDAR. Science, 335, 702–705. doi: 10.1126/science.1213778

Rollins, C., Barbot, S., Avouac, J.-P., 2015. Post-seismic deformation following the 2010 M = 7.2 El Mayor-Cucapah earthquake: observations, kinetic inversions, and dynamic models. Pure Appl Geophys. 172, 1305-1358. https://doi.org/10.1007/s00024-014-1005-6.

Rudolph, M. L., and M. Manga (2010), Mud volcano response to the 4 April 2010 El Mayor - Cucapah earthquake, J. Geophys. Res., 115, B12211, doi:10.1029/2010JB007737.

Spinler, J. C., R. A. Bennett, C. Walls, S. Lawrence, and J. J. González García (2015), Assessing long-term postseismic deformation following the M7.2 4 April 2010, El Mayor-Cucapah earthquake with implications for lithospheric rheology in the Salton Trough, J. Geophys. Res. Solid Earth, 120, 3664–3679, doi:10.1002/2014JB011613.

Stenner, H.D., Mathieson, E.L., Okubo, S., Anderson, R., Rodriguez C., M.A. 2010. Damage from the El Mayor-Cucapah earthquake, April 2010: Why society cannot afford to ignore seismic risks to agricultural regions. AGU Fall Meeting Abstracts 2010, T53B-2137.

Trugman, D. T., A. A. Borsa, and D. T. Sandwell (2014), Did stresses from the Cerro Prieto Geothermal Field influence the El Mayor-Cucapah rupture sequence? Geophys. Res. Lett., 41, 8767–8774, doi:10.1002/2014GL061959.

Uchide, T., H. Yao, and P. M. Shearer (2013), Spatio-temporal distribution of fault slip and high-frequency radiation of the 2010 El Mayor-Cucapah, Mexico earthquake, J. Geophys. Res. Solid Earth, 118, 1546–1555, doi:10.1002/jgrb.50144.

Wang, K., & Fialko, Y. (2018). Observations and modeling of coseismic and postseismic deformation due to the 2015 Mw 7.8 Gorkha (Nepal) earthquake. Journal of Geophysical Research: Solid Earth, 123, 761–779. https://doi.org/10.1002/2017JB014620

Wei, S., Fielding, E., Leprince, S. *et al.* Superficial simplicity of the 2010 El Mayor–Cucapah earthquake of Baja California in Mexico. *Nature Geosci* **4,** 615–618 (2011a). https://doi.org/10.1038/ngeo1213

Wei, M., D. Sandwell, Y. Fialko, and R. Bilham (2011b), Slip on faults in the Imperial Valley triggered by the 4 April 2010 Mw 7.2 El Mayor - Cucapah earthquake revealed by InSAR, Geophys. Res. Lett., 38, L01308, doi:10.1029/2010GL045235.

Zheng, Y., Li, J., Xie, Z., & Ritzwoller, M. H. (2012). 5 Hz GPS seismology of the El Mayor-Cucapah earthquake: Estimating the earthquake focal mechanism. Geophysical Journal International, 190, 1723–1732.

Captions

Fig 1. Map of the epicentral region of the El Mayor-Cucapah earthquake. Black dashed fault plane outlines represent the geometry from Huang17. Red line represents the actual fault trace while the positions of the actual fault segments are reported in blue. Red star is the epicenter location based on the Southern California Seismic Network (SCSN) catalog. Beach ball is the focal mechanism is from Zheng et al., 2012. In the inset, the tectonic overview of Southern California and Baja California including the Pacific–North America plate boundary and the California, Arizona and Mexico borders. The red dashed box corresponds to the main figure.

Fig 2. a) Model geometry. The main domain is represented by a volume of 540x440x150 km, surrounded by a frame of 5 km thick domains with infinite elements. A 9-segment fault system is embedded into it. b) Layered configuration with four different layers. Color scale represents the values of Young's modulus (GPa). Model topography is also shown at the model top surface. c) Young's modulus (GPa) in a heterogeneous configuration. d) Poisson's ratio in a heterogeneous configuration.

Fig 3. a) Model mesh. The model volume is discretized with tetrahedral elements while triangular elements are used for the surfaces. The inset at the bottom right corner shows the mesh near the fault trace. b) Inside view of the model

mesh showing the discretization on the fault segments. Eight NW-SE aligned fault segments are discretized using quadrilateral elements while triangular elements are used for the transversal one.

Figure 4. a) Comparison between the GPS horizontal (vectors) and vertical (circles with associated color scale) displacement components obtained using Huang17 solution (red vectors and inner circles) vs measurements (black vectors and outer circles). Black line represents the fault trace. b) Huang17 solution horizontal displacement (black solid line) and vertical displacement (black dashed line) versus measured horizontal displacement (red solid line) and measured vertical displacement (red dashed line).

Figure 5. a) Comparison between the GPS horizontal (vectors) and vertical (circles with associated color scale) displacement components for the optimized solution in the homogenous case (red vectors inner circles) and the measured data (black vectors, outer circles). Black line represents the fault trace. b) Optimized solution horizontal displacement (black solid line) and vertical displacement (black dashed line) versus measured horizontal displacement (red solid line) and measured vertical displacement (red dashed line).

Figure 6. **a)** Horizontal (vectors) and vertical (circles with associated color scale) GPS displacement components. Recorded (black), optimized homogeneous (red), optimized layered (blue), optimized heterogeneous (gray). The outermost to innermost circle follow the order of the legend from top to bottom. Black line represents the fault trace. b) Residuals of the horizontal and vertical homogeneous minus layered solutions (black vectors outer circles) and homogeneous minus heterogeneous solutions (red vectors inner circles).

Figure 7. a) Horizontal (vectors) and vertical (circles) GPS displacement components. Dashed white line represents the northern border of Salton Trough area. Recorded (black), optimized homogeneous (red), optimized layered (blue), optimized heterogeneous (gray). The outermost to innermost circle follow the order of the legend from top to bottom. b) Residuals of homogeneous minus layered (black vectors, outer circle) and homogeneous minus heterogeneous solutions (red vectors, inner circle).

Figure 8. Measured (a,d), modeled homogeneous (b,e) and residuals (c,f) output for the InSAR data, ascending (top row) and descending (bottom row) tracks. Black line represents the fault trace.

Figure 9. Residuals from the numerical solutions. a) ascending homogeneous-layered; b) ascending homogeneous - heterogeneous; c) descending homogeneous-layered; d) descending homogeneous- heterogeneous. Black line represents the fault trace.

Figure 10. Measured (a,d), modeled homogeneous (b,e) and residuals (c,f) output for the subpixel offset data EW (top row) and NS (bottom row) components. Black line represents the fault trace.

Figure 11. Residual from the numerical solutions for the subpixel offset data. a) homogeneous-layered EW component; b) homogeneous-heterogeneous EW component; c) homogeneous-layered NS component; d) homogeneous-heterogeneous NS component. Black line represents the fault trace.

571 **Figure 12**. Slip distributions. a) Huang17 solution with plane 9 in the inset; b) Optimized solution in the homogeneous
572 case; c) Optimized solution in the layered case; d) Optimized solution in the heterogeneous case). Inset is excluded
573 from b, c and d as it is the same of a. Actual fault names and positions are shown in blue.

574 **Figure 13**. Residuals of the slip distribution from the different cases of the joint inversion. a) Homogeneous-Huang17
575 solution. b) Layered-Homogeneous. c) Heterogeneous-Homogeneous. d) Layered-Heterogeneous.

576 **Figure 14**. Optimized slip distribution in a homogeneous domain obtained using Huang17 solution as starting slip in all
577 planes except plane 8, where one meter uniform starting slip is applied.

578 **Figure 15**. Comparison between the horizontal (vectors) and vertical (circles) displacements at the western GPS
579 stations obtained from the measured data (black vectors) and the optimized solution with deeper slip (red vectors) and
580 intermediate slip (blue vectors) on the southernmost plane. The outermost to innermost circle follow the order of the
581 legend from top to bottom. Red dashed rectangle represents the position of the southernmost plane.

582 **Figure 16**. Residuals between measurements and the homogeneous joint inversion for the InSAR data with deeper (a, c)
583 and intermediate slip (b, d) on plane 8 for the ascending (top row) and descending (bottom row) tracks.

Tables

Table 1. Model material parameters in the homogeneous, layered and fully heterogeneous cases.

Homogeneous Model	Depth (km)	Shear modulus (GPa)	Poisson's ratio
	0-150	24.3	0.25
Layered Model	Depth (km)	Shear modulus (GPa)	Poisson's ratio
	0 - 5.5	24.3	0.25
	5.5 - 16.0	35.4	
	16.0 - 32.0	41.9	
	32.0 - 150	60.7	
Heterogeneous Model	Depth (km)	Shear modulus (GPa)	Poisson's ratio
	0 - 150	24 - 72	0.25-0.32

Table 2. Total, horizontal and vertical standard deviations for the analytical and numerical solutions (optimized) at the selected GPS stations.

Solution	**σ_tot**	**σ_horizontal**	**σ_vertical**
Huang17	0.112	0.108	0.123
FEM Homogeneous	0.057	0.048	0.074
FEM Layered	0.057	0.050	0.070
FEM Heterogeneous	0.058	0.052	0.070

Table 3. Total standard deviations for the analytical (homogeneous case) and numerical solutions (optimized) for the InSAR ascending and descending tracks.

InSAR Ascending Track	**σ_tot**	**InSAR Descending Track**	**σ_tot**
Huang17	0.128	Huang17	0.060
FEM Homogeneous	0.070	FEM Homogeneous	0.047
FEM Layered	0.072	FEM Layered	0.047
FEM Heterogeneous	0.072	FEM Heterogeneous	0.048

Table 4. Total, EW and NS standard deviations for the analytical (homogeneous case) and numerical solutions (optimized) for the subpixel offset dataset.

Subpixel offset solution	**σ_tot**	**σ_E-W**	**σ_N-S**
Huang17	0.327	0.392	0.246
FEM Homogeneous	0.293	0.329	0.254
FEM Layered	0.290	0.322	0.255
FEM Heterogeneous	0.290	0.321	0.255

Table 5. Moment magnitude from the not optimized (Huang et al. 2017), the optimized (FEM) and the Southern California Seismic Network Solution.

Material configuration	**M_w Huang17**	**M_w FEM**	**GCMT**
Homogeneous	7.26	7.24	7.20
Layered	7.32	7.33	
Heterogeneous	N/A	7.36	

Figure 1.

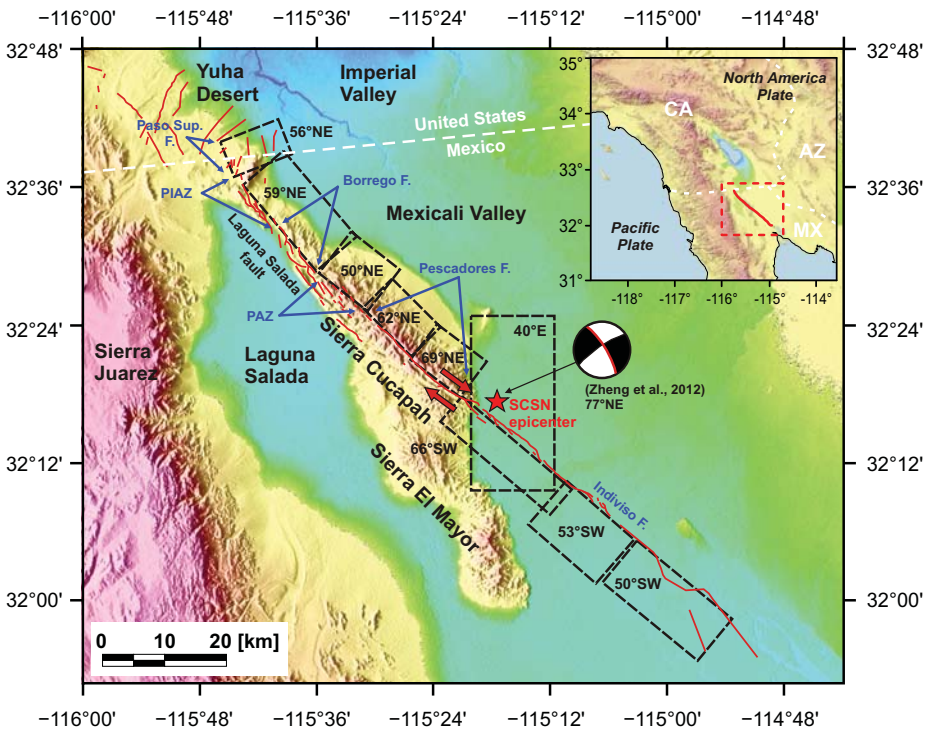
−116°00'
−115°48'
−115°36'
−115°24'
−115°12'
−115°00'
−114°48'
32°48'
32°36'
32°24'
32°12'
32°00'
Yuha Desert
Imperial Valley
United States
Mexico
Paso Sup. F.
56°NE
PIAZ
59°NE
Borrego F.
Mexicali Valley
Laguna Salada fault
50°NE
Pescadores F.
PAZ
62°NE
69°NE
40°E
Sierra Juarez
Laguna Salada
Sierra Cucapah
Sierra El Mayor
66°SW
SCSN epicenter
(Zheng et al., 2012)
77°NE
Indiviso F.
53°SW
50°SW
0 10 20 [km]
North America Plate
Pacific Plate
CA
AZ
MX
35°
34°
33°
32°
31°
-118°
-117°
-116°
-115°
-114°

Figure 2.

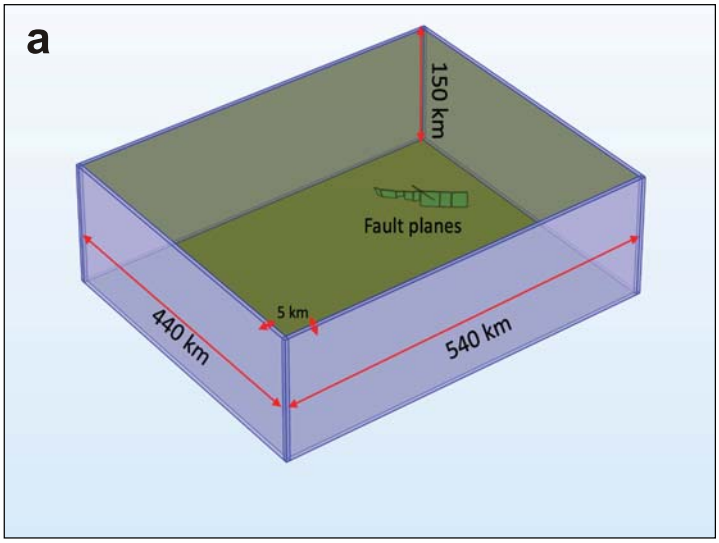
a
150 km
Fault planes
5 km
440 km
540 km

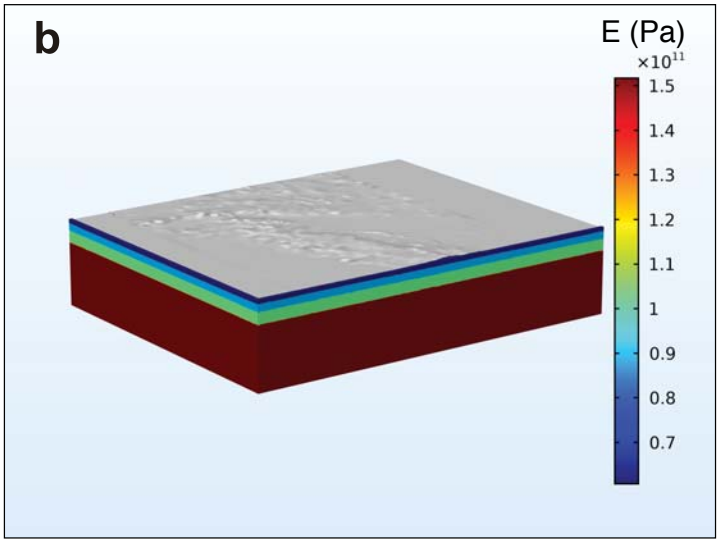
b
E (Pa)
×10^11
1.5
1.4
1.3
1.2
1.1
1
0.9
0.8
0.7

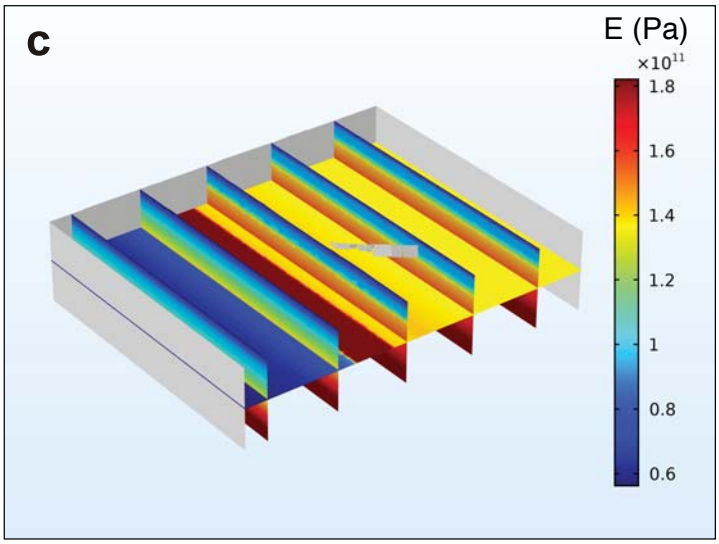
c
E (Pa)
×10^11
1.8
1.6
1.4
1.2
1
0.8
0.6

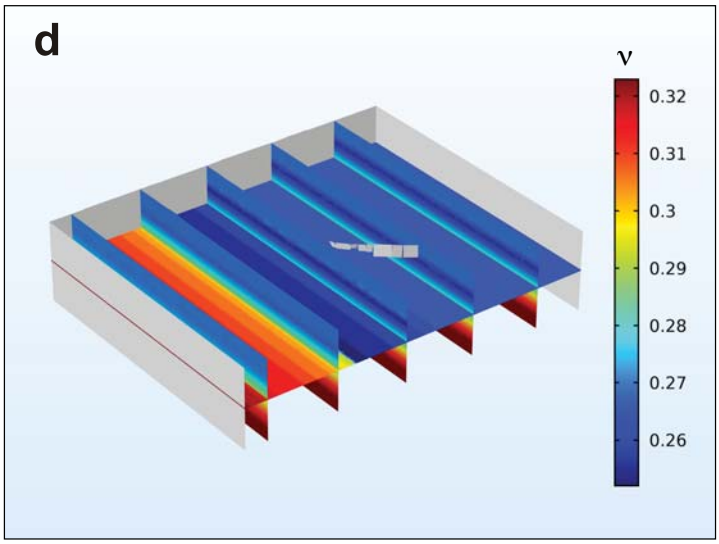
d
ν
0.32
0.31
0.3
0.29
0.28
0.27
0.26

Figure 3.

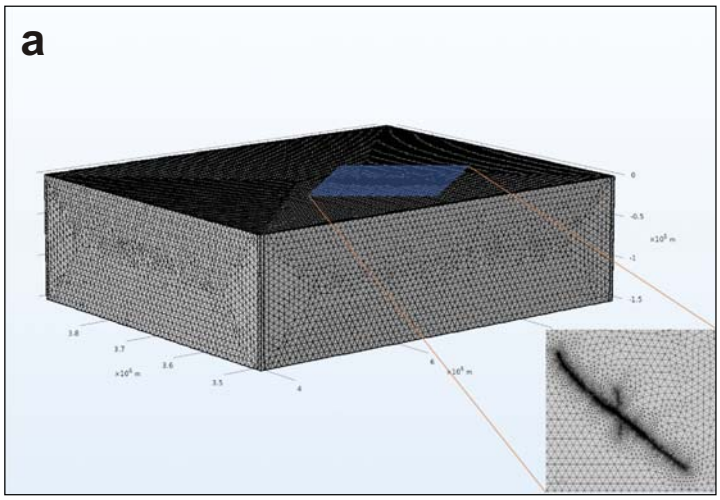
a
0
-0.5
-1
-1.5
3.8
3.7
3.6
3.5
4
6

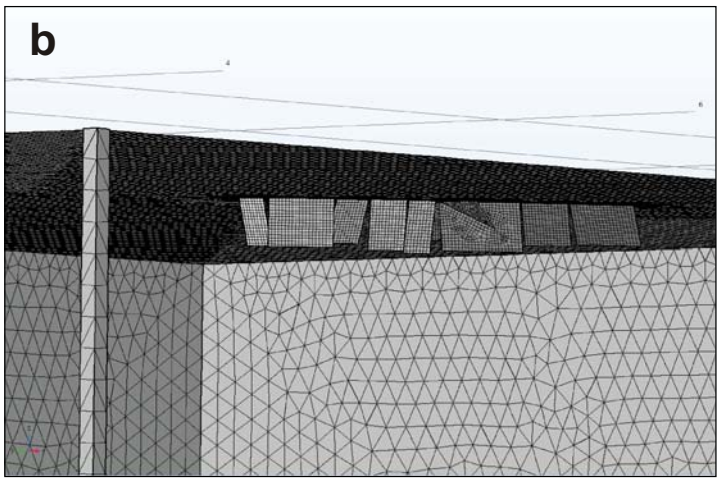
b
4
6

Figure 4.

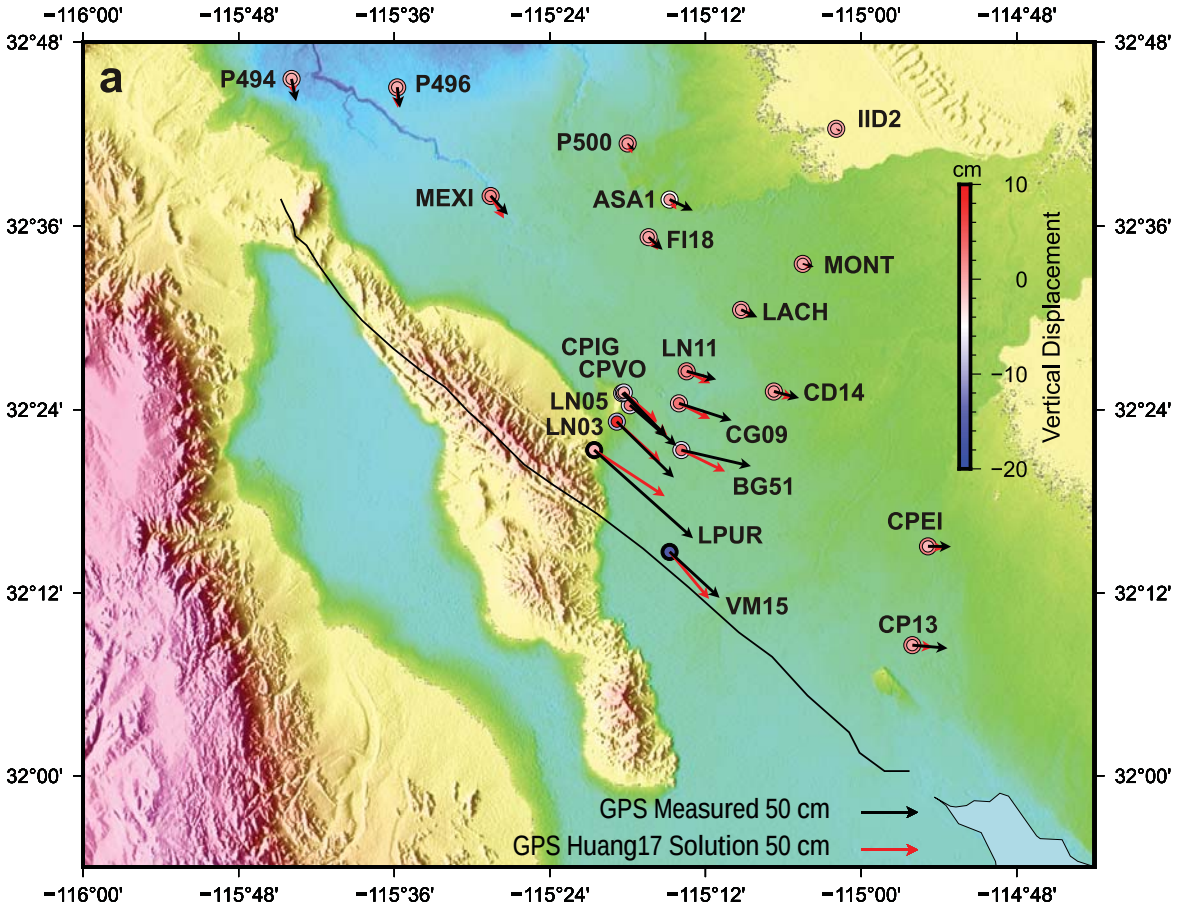
a
−116°00'
−115°48'
−115°36'
−115°24'
−115°12'
−115°00'
−114°48'
32°48'
32°36'
32°24'
32°12'
32°00'
P494
P496
IID2
P500
MEXI
ASA1
FI18
MONT
LACH
CPIG
CPVO
LN11
LN05
LN03
CD14
CG09
BG51
LPUR
CPEI
VM15
CP13
cm
10
0
−10
−20
Vertical Displacement
GPS Measured 50 cm
GPS Huang17 Solution 50 cm

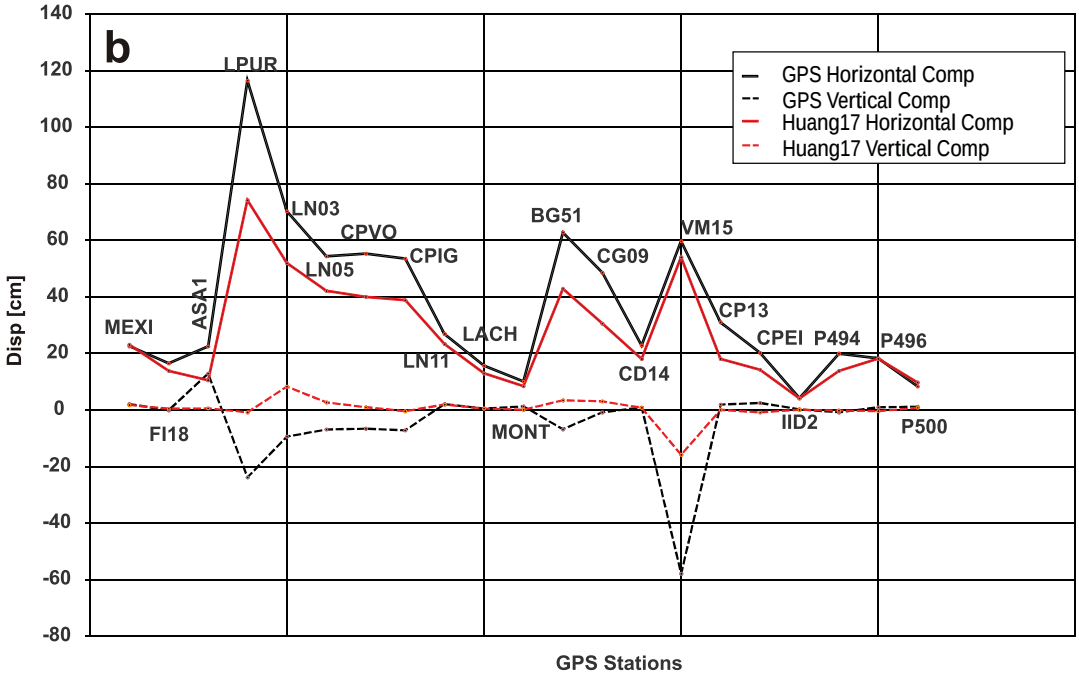
b
140
120
100
80
60
40
20
0
-20
-40
-60
-80
Disp [cm]
GPS Stations
GPS Horizontal Comp
GPS Vertical Comp
Huang17 Horizontal Comp
Huang17 Vertical Comp
MEXI
ASA1
FI18
LPUR
LN03
CPVO
CPIG
LN05
LN11
LACH
MONT
BG51
CG09
CD14
VM15
CP13
CPEI
P494
IID2
P496
P500

Figure 5.

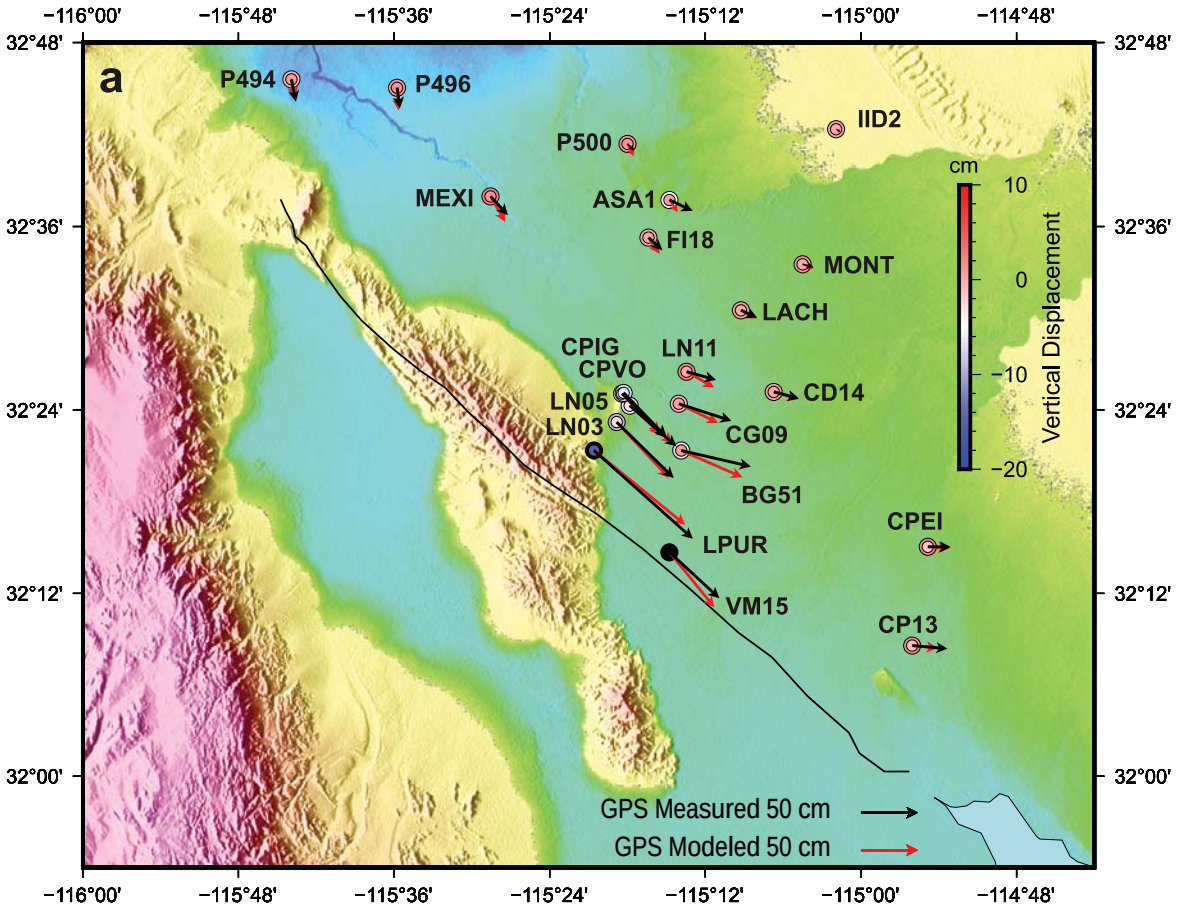
a
−116°00'
−115°48'
−115°36'
−115°24'
−115°12'
−115°00'
−114°48'
32°48'
32°36'
32°24'
32°12'
32°00'
P494
P496
IID2
P500
MEXI
ASA1
FI18
MONT
LACH
CPIG
CPVO
LN11
LN05
LN03
CD14
CG09
BG51
LPUR
CPEI
VM15
CP13
cm
10
0
−10
−20
Vertical Displacement
GPS Measured 50 cm
GPS Modeled 50 cm

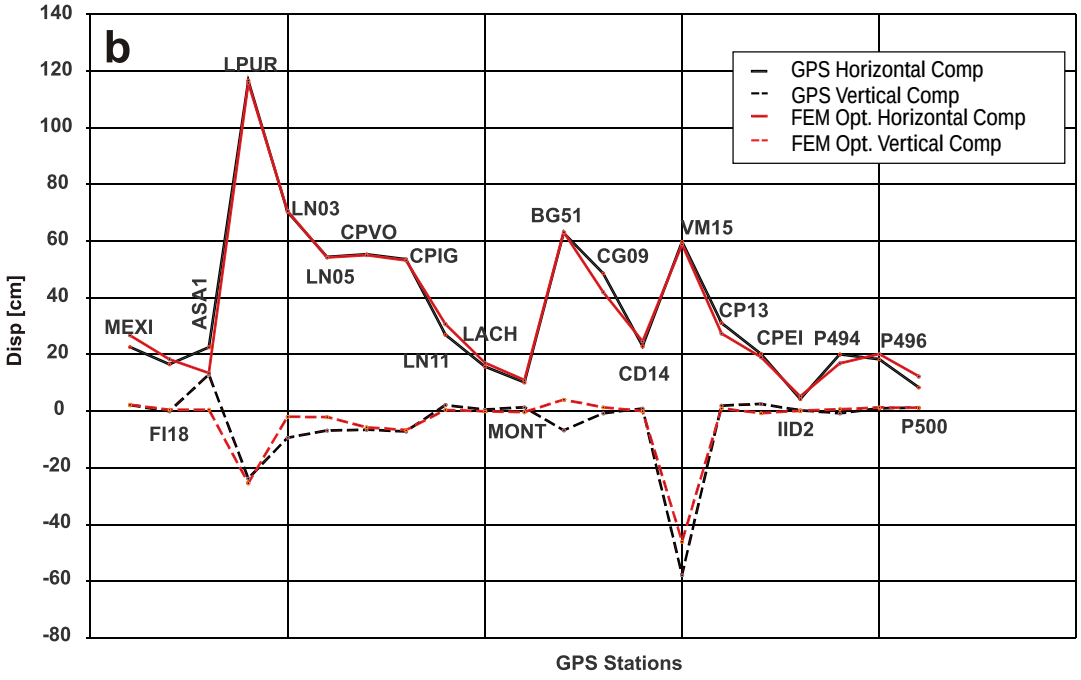
b
GPS Horizontal Comp
GPS Vertical Comp
FEM Opt. Horizontal Comp
FEM Opt. Vertical Comp
Disp [cm]
GPS Stations
140
120
100
80
60
40
20
0
-20
-40
-60
-80
MEXI
ASA1
LPUR
LN03
CPVO
CPIG
LN05
LACH
LN11
FI18
BG51
CG09
MONT
CD14
VM15
CP13
CPEI
P494
P496
IID2
P500

Figure 6.

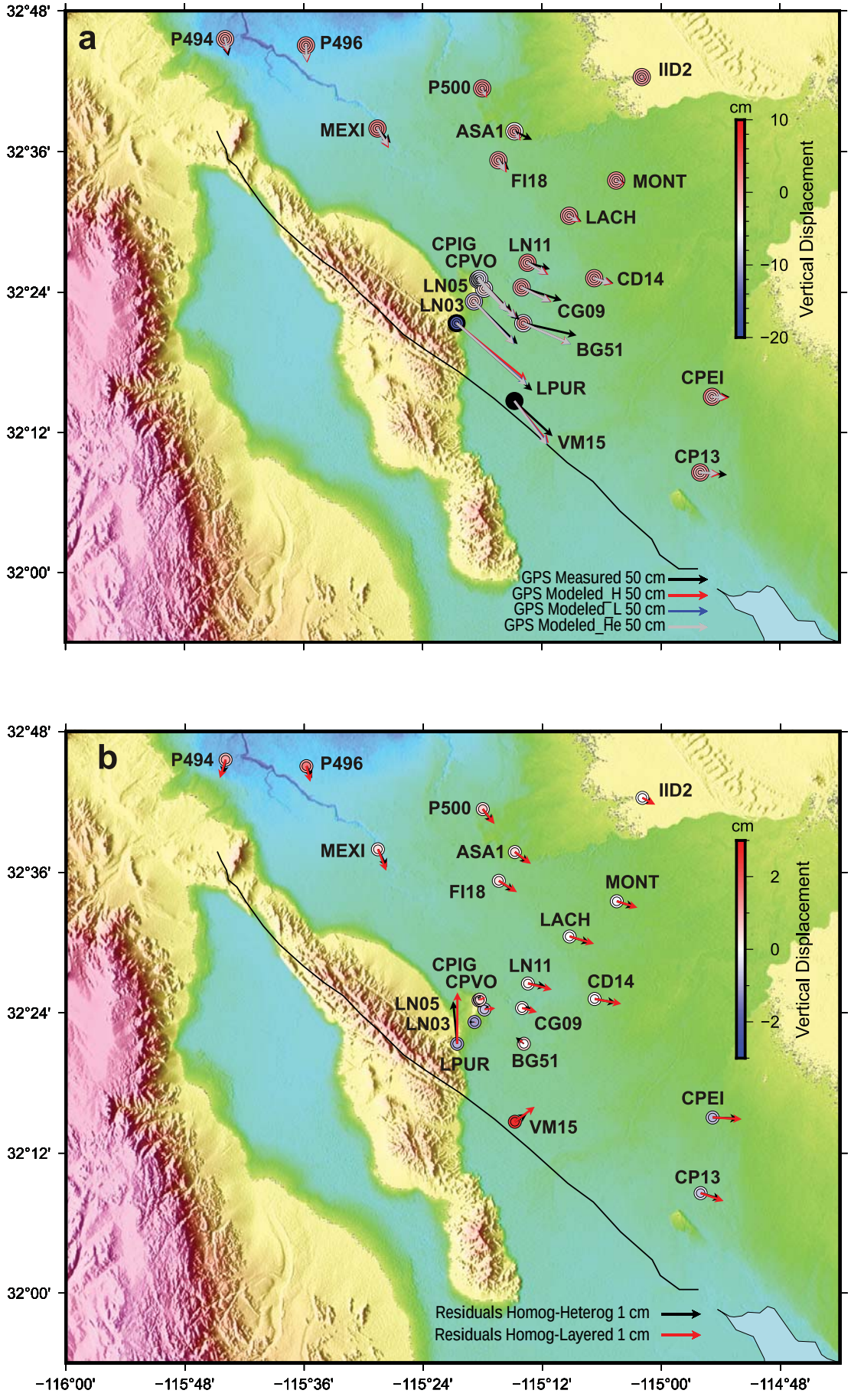
a
P494
P496
IID2
P500
MEXI
ASA1
FI18
MONT
LACH
CPIG
CPVO
LN11
CD14
LN05
LN03
CG09
BG51
LPUR
CPEI
VM15
CP13
cm
10
0
−10
−20
Vertical Displacement
32°48'
32°36'
32°24'
32°12'
32°00'
GPS Measured 50 cm
GPS Modeled_H 50 cm
GPS Modeled_L 50 cm
GPS Modeled_He 50 cm
b
P494
P496
IID2
P500
MEXI
ASA1
FI18
MONT
LACH
CPIG
CPVO
LN11
CD14
LN05
LN03
CG09
LPUR
BG51
CPEI
VM15
CP13
cm
2
0
−2
Vertical Displacement
32°48'
32°36'
32°24'
32°12'
32°00'
Residuals Homog-Heterog 1 cm
Residuals Homog-Layered 1 cm
−116°00'
−115°48'
−115°36'
−115°24'
−115°12'
−115°00'
−114°48'

Figure 7.

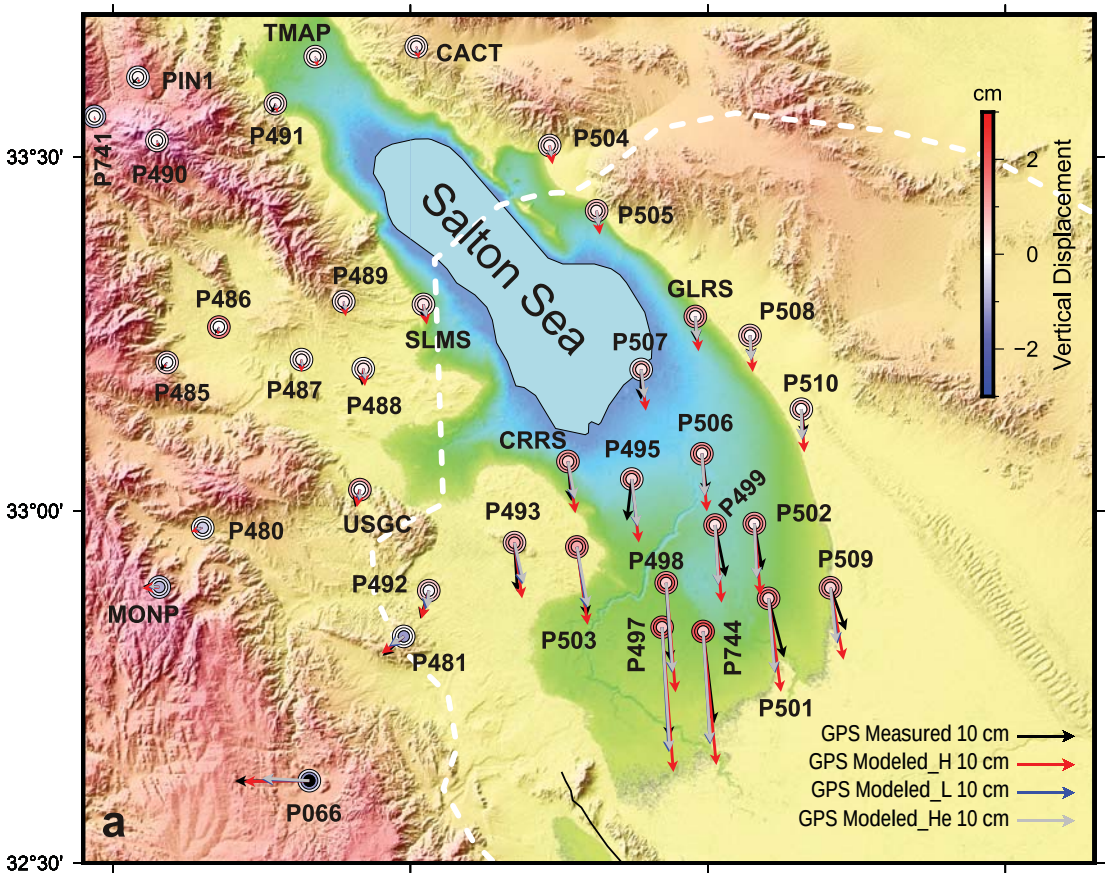
TMAP
CACT
PIN1
P491
P741
P490
P504
P505
Salton Sea
P489
P486
SLMS
GLRS
P508
P507
P485
P487
P488
P510
P506
CRRS
P495
P499
P493
USGC
P502
P480
P498
P509
P492
MONP
P503
P497
P744
P481
P501
P066
a
33°30'
33°00'
32°30'
cm
2
0
−2
Vertical Displacement
GPS Measured 10 cm
GPS Modeled_H 10 cm
GPS Modeled_L 10 cm
GPS Modeled_He 10 cm

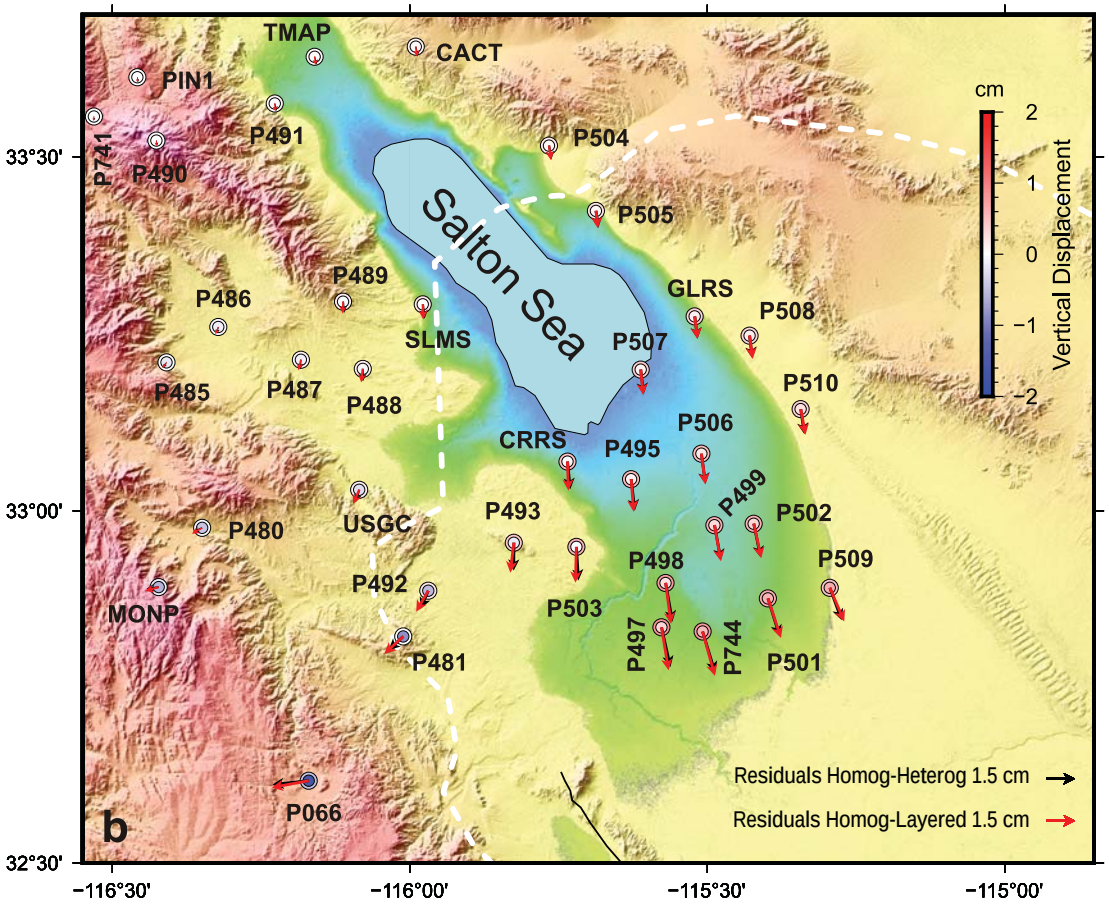
TMAP
CACT
PIN1
P491
P741
P490
P504
P505
Salton Sea
P489
P486
SLMS
GLRS
P508
P507
P485
P487
P488
P510
P506
CRRS
P495
P499
P493
USGC
P502
P480
P498
P509
P492
MONP
P503
P497
P744
P481
P501
P066
b
33°30'
33°00'
32°30'
−116°30'
−116°00'
−115°30'
−115°00'
cm
2
1
0
−1
−2
Vertical Displacement
Residuals Homog-Heterog 1.5 cm
Residuals Homog-Layered 1.5 cm

Figure 8.

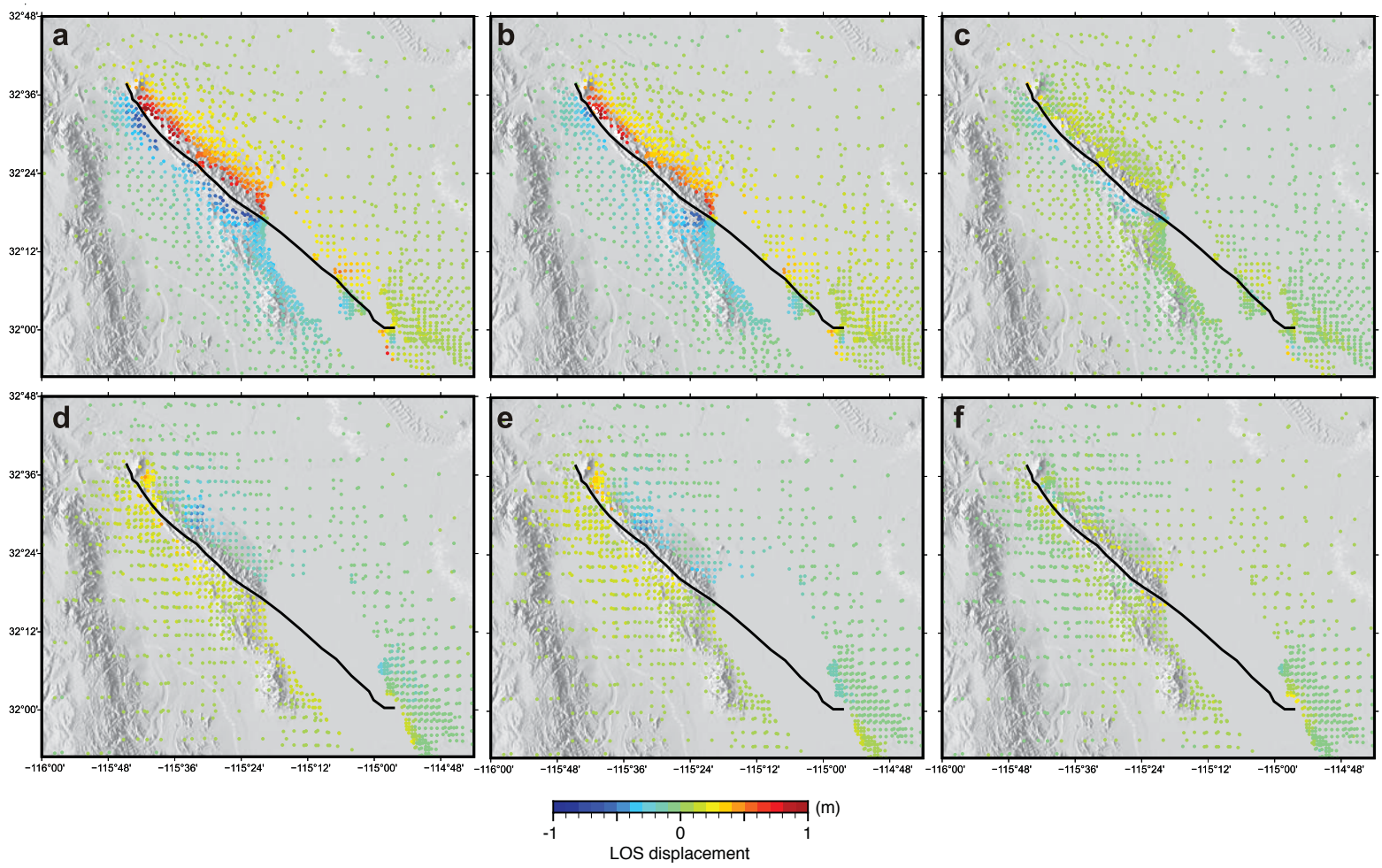
a
b
c
d
e
f
32°48'
32°36'
32°24'
32°12'
32°00'
−116°00'
−115°48'
−115°36'
−115°24'
−115°12'
−115°00'
−114°48'
-1
0
1
(m)
LOS displacement

Figure 9.

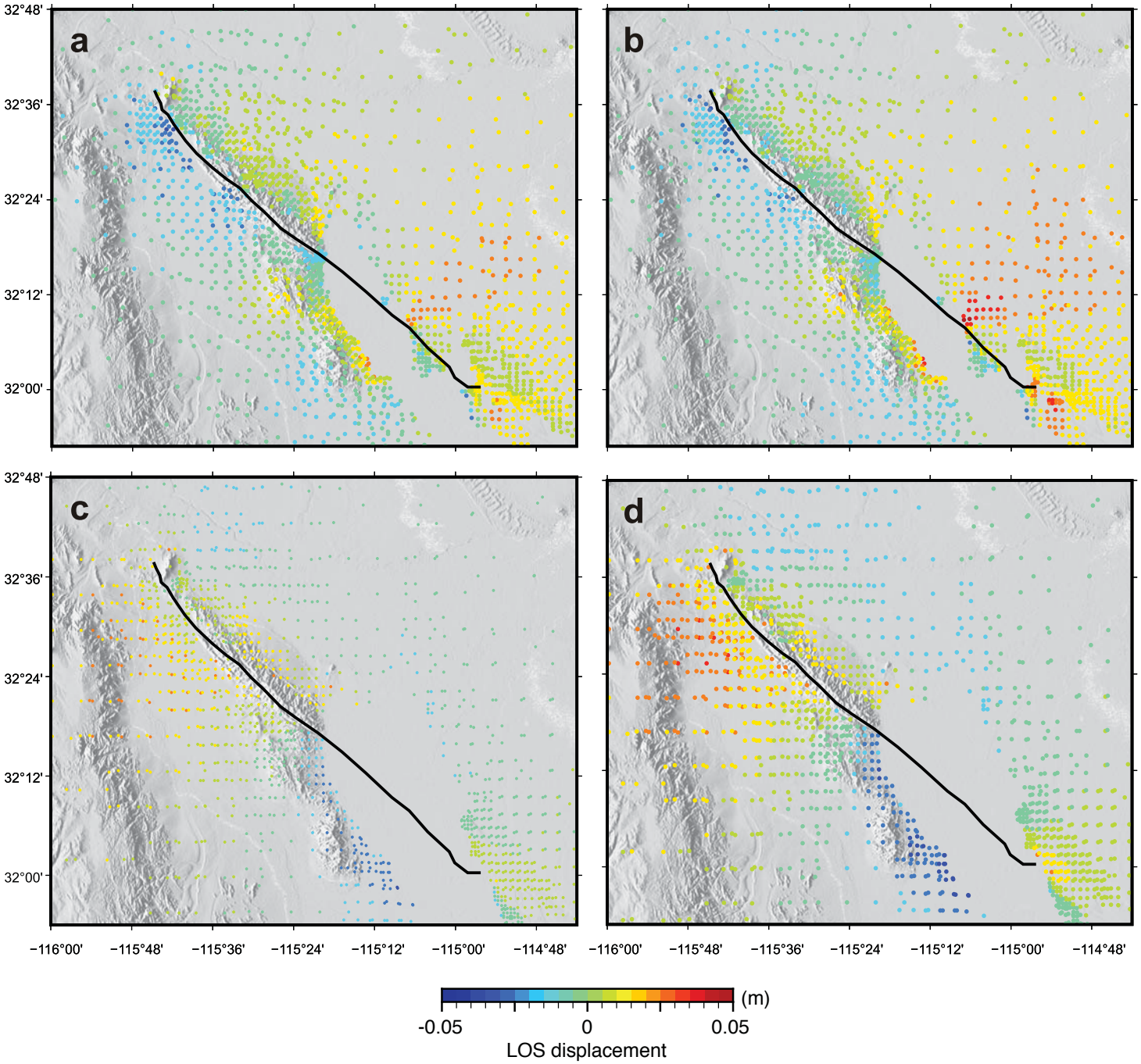
a
b
c
d
32°48'
32°36'
32°24'
32°12'
32°00'
−116°00'
−115°48'
−115°36'
−115°24'
−115°12'
−115°00'
−114°48'
(m)
-0.05
0
0.05
LOS displacement

Figure 10.

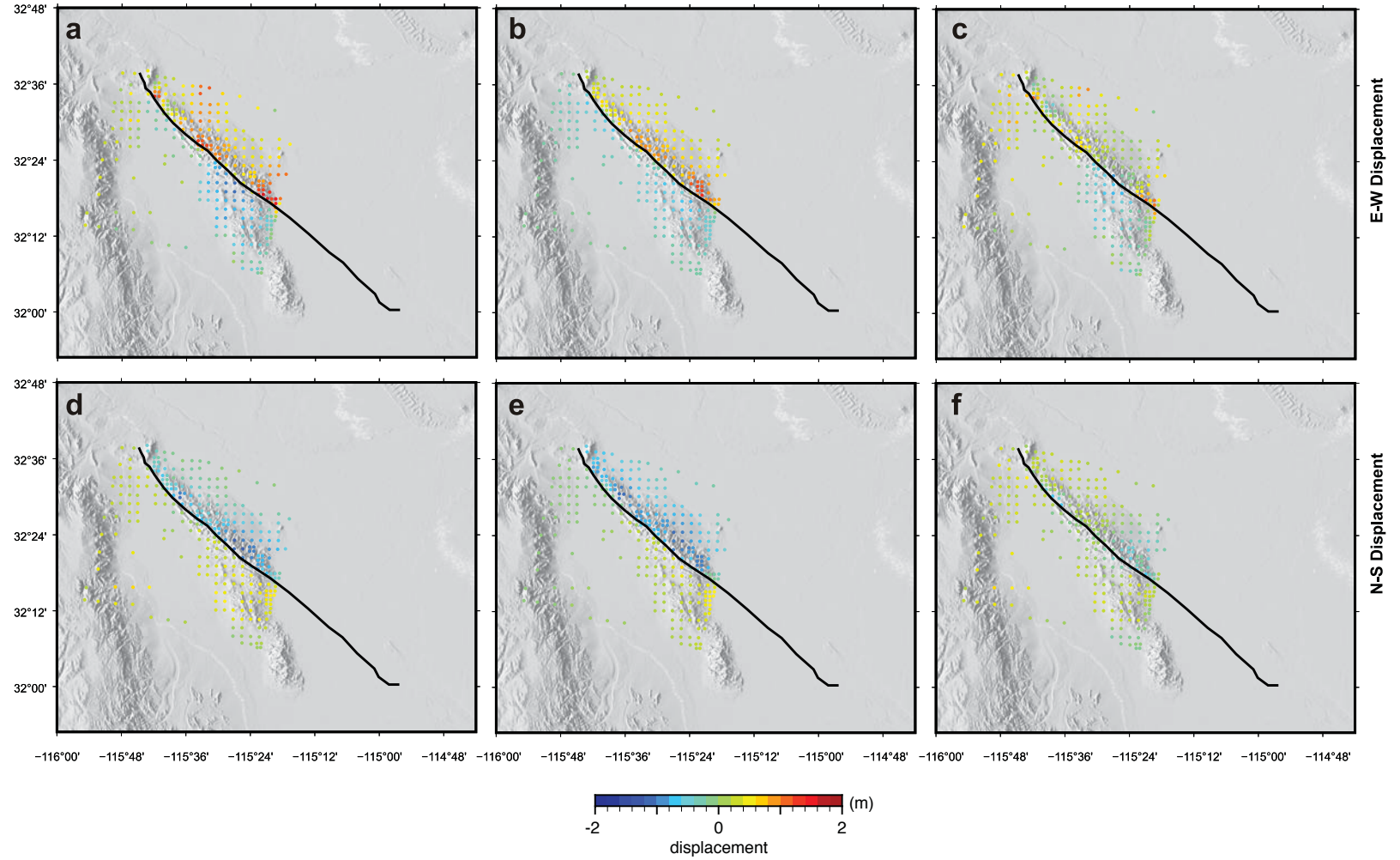
a
b
c
d
e
f
32°48'
32°36'
32°24'
32°12'
32°00'
−116°00'
−115°48'
−115°36'
−115°24'
−115°12'
−115°00'
−114°48'
E-W Displacement
N-S Displacement
(m)
-2
0
2
displacement

Figure 11.

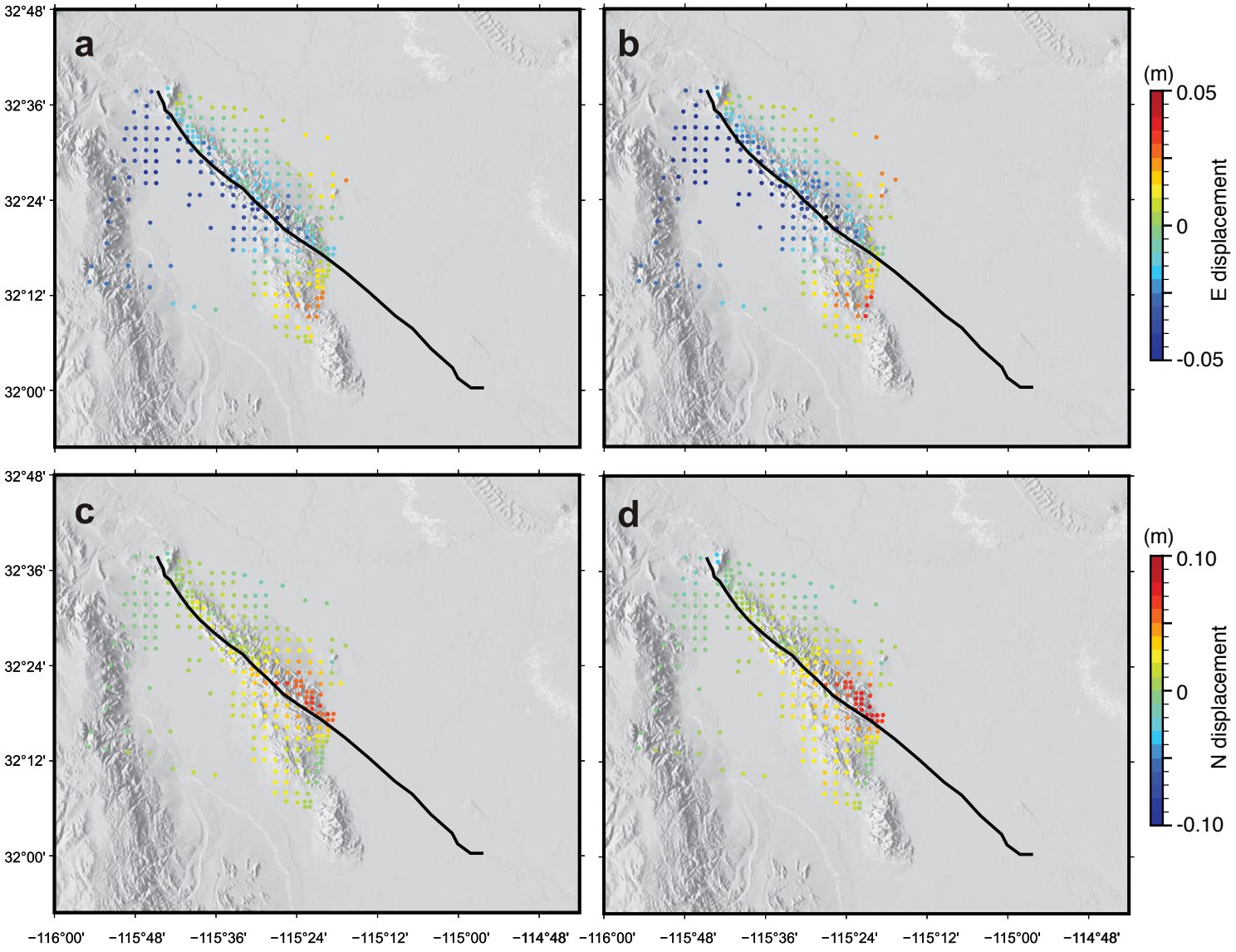
a
b
c
d
32°48'
32°36'
32°24'
32°12'
32°00'
−116°00'
−115°48'
−115°36'
−115°24'
−115°12'
−115°00'
−114°48'
(m)
0.05
0
-0.05
E displacement
(m)
0.10
0
-0.10
N displacement

Figure 12.

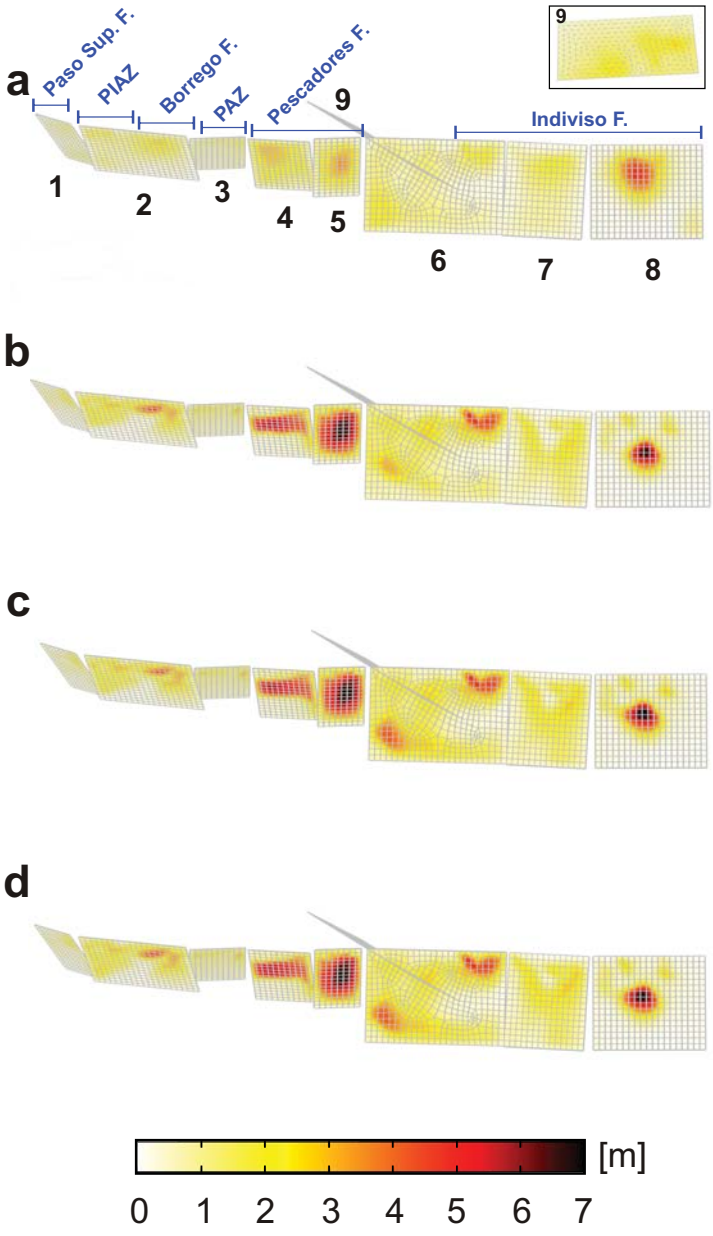
a
Paso Sup. F.
PIAZ
Borrego F.
PAZ
Pescadores F.
9
Indiviso F.
1
2
3
4
5
6
7
8
9
b
c
d
[m]
0 1 2 3 4 5 6 7

Figure 13.

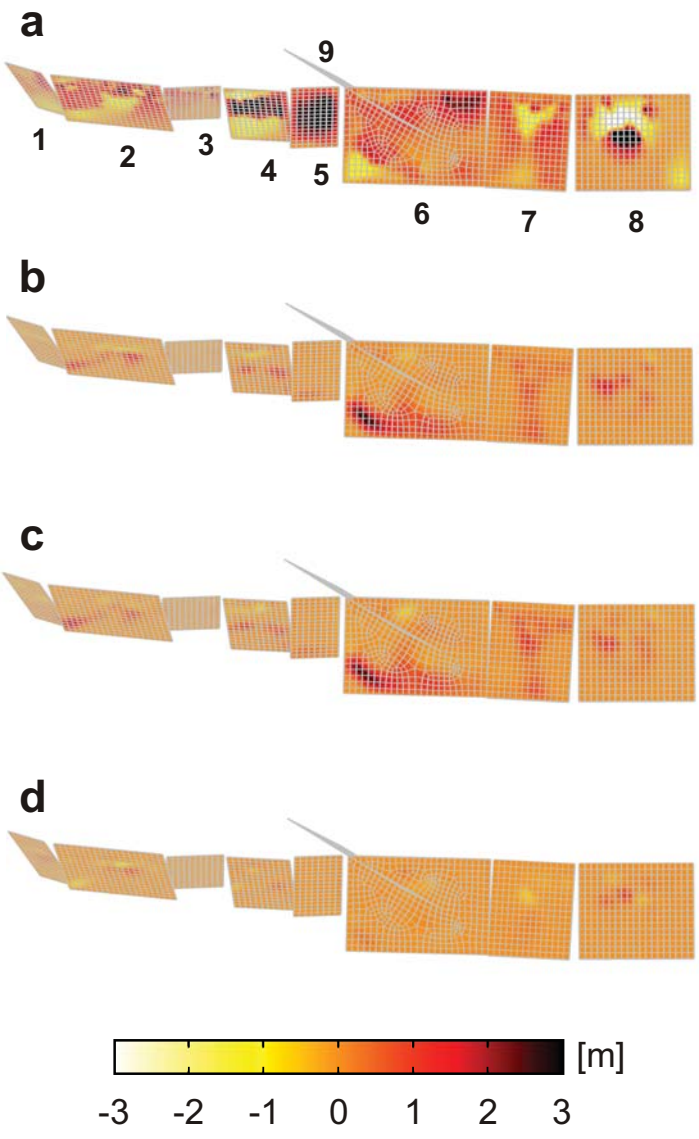
a
1
2
3
4
5
9
6
7
8
b
c
d
[m]
-3
-2
-1
0
1
2
3

Figure 14.

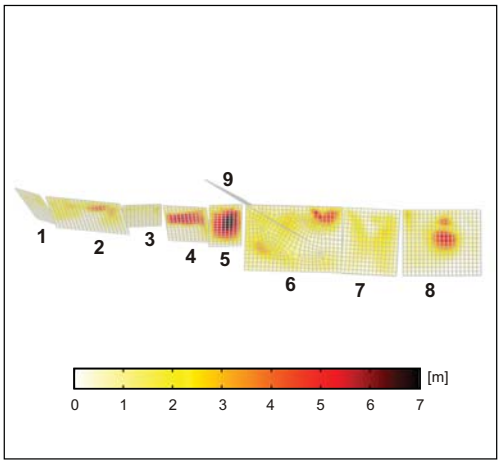
9
1
2
3
4
5
6
7
8
[m]
0
1
2
3
4
5
6
7

Figure 15.

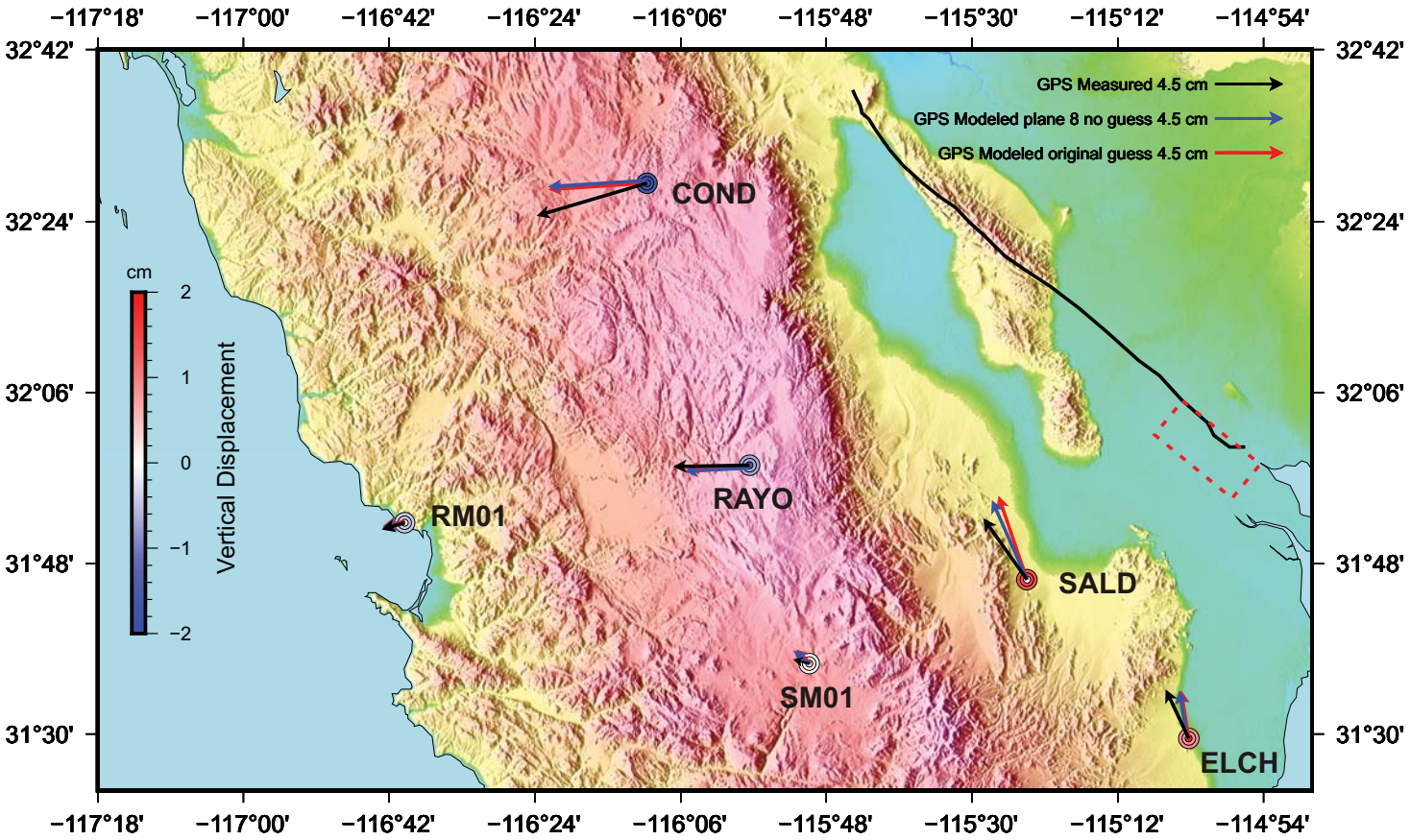
−117°18'
−117°00'
−116°42'
−116°24'
−116°06'
−115°48'
−115°30'
−115°12'
−114°54'
32°42'
32°24'
32°06'
31°48'
31°30'
GPS Measured 4.5 cm
GPS Modeled plane 8 no guess 4.5 cm
GPS Modeled original guess 4.5 cm
cm
2
1
0
−1
−2
Vertical Displacement
COND
RAYO
RM01
SALD
SM01
ELCH

Figure 16.

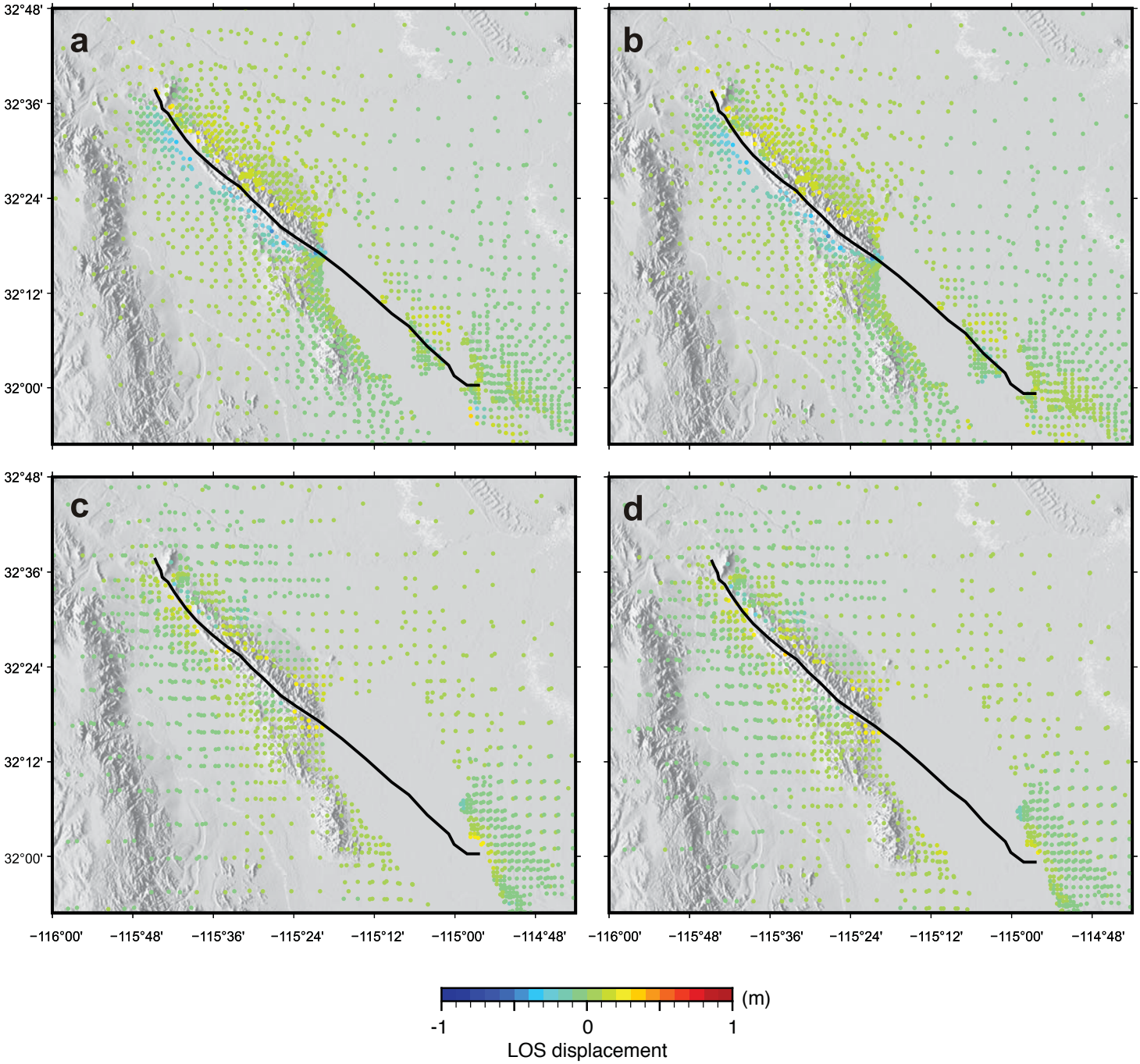
a
b
c
d
32°48'
32°36'
32°24'
32°12'
32°00'
−116°00'
−115°48'
−115°36'
−115°24'
−115°12'
−115°00'
−114°48'
(m)
-1
0
1
LOS displacement